Alignment-induced self-organization of autonomously steering microswimmers: Turbulence, clusters, vortices, and jets

Segun Goh [1], Elmar Westphal [2], Roland G. Winkler [1], and Gerhard Gompper [1,*]

[1] *Theoretical Physics of Living Matter, Institute for Advanced Simulation, Forschungszentrum Jülich, 52425 Jülich, Germany*

[2] *Peter Grünberg Institute and Jülich Centre for Neutron Science, Forschungszentrum Jülich, 52425 Jülich, Germany*

(Received 10 July 2024; accepted 17 January 2025; published 7 February 2025)

Microorganisms can sense their environment and adapt their movement accordingly, which gives rise to a multitude of collective phenomena, including active turbulence and bioconvection. In fluid environments, collective self-organization is governed by hydrodynamic interactions. By large-scale mesoscale hydrodynamics simulations, we study the collective motion of polar microswimmers, which align their propulsion direction by hydrodynamic steering with that of their neighbors. The simulations of the employed squirmer model reveal a distinct dependence on the type of microswimmer—puller or pusher—flow field. No global polar alignment emerges in both cases. Instead, the collective motion of pushers is characterized by active turbulence, with nearly homogeneous density and a Gaussian velocity distribution; strong self-steering enhances the local coherent movement of microswimmers and leads to local fluid-flow speeds much larger than the individual swim speed. Pullers exhibit a strong tendency for clustering and display velocity and vorticity distributions with fat exponential tails; their dynamics is chaotic, with a temporal appearance of vortex rings and fluid jets. Our results show that the collective behavior of autonomously steering microswimmers displays a rich variety of dynamic self-organized structures. Our results imply guidelines for the design of microrobotic systems.

DOI: 10.1103/PhysRevResearch.7.013142

I. INTRODUCTION

The emergence of dynamic structures and patterns is an essential feature of biological active motile systems. Examples include microbial swarms [1,2] on the cellular level as well as schools of fish [3,4], flocks of birds [5,6], and the collective motion in human crowds [7] on a macroscopic level. Also, in artificial active systems consisting of synthetic self-propelled particles and microrobots, the collective dynamics of the constituent objects is of prime importance for their application in engineering and medicine to achieve a large spectrum of functionalities [8–11].

A fundamental aspect in such systems is the active and autonomous motion of the constituting particles [12–16]. While activity and self-propulsion can give rise to several types of collective behaviors, such as motility-induced phase separation (MIPS) [17,18] and active turbulence [19–21], the fact that biological microswimmers are not only motile but also gather information about their environment and adapt their motion through self-steering remains largely unexplored and has yet to be elucidated [22–24]. Similar physical laws also govern the swarming of microrobots [8,25].

Many living organisms are immersed in a fluid medium, and their collective behavior is strongly affected or even dominated by hydrodynamics [12–14]. The hydrodynamic environment is not just the background medium in which aquatic microorganisms are based, but it is rather essential for locomotion on the individual level as well as interorganism interactions [1,26,27]. Fluid-mediated interactions at low Reynolds numbers lead to intriguing emergent behaviors such as bacterial turbulence [21,28–30] and coordinated cell migration during embryogenesis [31,32].

In thin films, experiments on bacteria suspensions [21,29,30,33] and simulations of polar active fluids [19,20,34] have revealed chaotic dynamics and the presence of vortices. The characterization of the mesoscale turbulence in terms of Kolmogorov's energy spectrum function [35] shows that the behavior depends on the constituents of the systems and the detailed (microscopic) interaction mechanisms [20,21,30]. The presence of surfaces [36] and the type of microswimmer flow field, such as the presence of a rotlet dipole by the counterrotation of the cell body and flagellar bundle of bacteria, can be paramount for the emergent collective motion [20].

Far less is known about the collective and turbulent dynamics of microswimmers in three dimensions, although hydrodynamic interactions are essential for various phenomena in aquatic microbial systems, such as bioconvection [37,38], blooms of cyanobacteria [39] or dinoflagellates [40], or phytoplankton migration in turbulent flows [41].

The goal of our current endeavor is to unravel the emergent collective behavior of systems in three spatial dimensions, which combine two essential components of living and artificial active systems, self-steering and hydrodynamics.

*Contact author: g.gompper@fz-juelich.de

Accurate modeling of swarms of locally aligning microorganisms or microrobots is extremely challenging, as they usually involve complicated cell-cell signaling or interparticle communication. Here, simple models facilitate the understanding of the universal aspects of their dynamics in terms of symmetries and instabilities [19,42,43], without an overload of possibly irrelevant details. In the context of active matter, the model of aligning active particles by Vicsek *et al.* [44] has been frequently employed to study the emergence of long-range order in collective directional motion of self-steering particles [16].

While the role of alignment interactions has been extensively investigated for dry active systems [16], far less is known about wet polar active matter. In many cases, hydrodynamic interactions are viewed as a physical alignment mechanism in wet systems [45–47]. However, hydrodynamic propulsion can in fact also destabilize global polar order for extensile swimmers (pushers) [43,48]. Similarly, hydrodynamic interactions disturb local alignment [26,27,49]. Based on mostly phenomenological field-theoretical approaches, the instability of homogeneous ordered and disordered phases has been addressed, and the possible emergence of chaotic dynamics has been predicted [19,21,43,48,50]. However, general symmetry considerations may miss the underlying mechanism of collective behavior, when the universality of the dynamics is not guaranteed, as is the case for polar active turbulence [30]. Indeed, which form of self-organization will occur in wet aligning systems, beyond a stability analysis, is yet to be disclosed, particularly in three dimensions. Experimental studies on the coordinated migration of microorganisms have revealed heterogeneous and turbulent dynamic patterns, e.g., in bacterial turbulence [19], photobioconvection [37], or autochemotaxis [51]. Here, suitable microscopic models, capturing essential details of polar active fluids, can display nontrivial large-scale collective phenomena relevant for pattern formation in living systems.

Based on a model of self-steering, intelligent microswimmers [52], we propose a hydrodynamic version of the Vicsek model, which can generate local alignment in polar active fluids. This model can serve as a reference system for the self-organization in intelligent polar active fluids. Our active agents, modeled as squirmers [49,53–56], sense the propulsion direction of neighboring agents and adapt their propulsion direction accordingly by hydrodynamic self-steering [52,57], with a slow temporal response due to limited maneuverability. We perform large-scale simulations of three-dimensional systems, capturing the fluid environment by the multiparticle collision dynamics (MPC) technique [58–60], a particle-resolved mesoscale hydrodynamic simulation approach.

We observe and characterize the emergent swarming dynamics in polar active fluids. With hydrodynamic interactions, active stress becomes relevant, and pusher and puller microswimmers are expected to behave qualitatively different. Our results show that hydrodynamic interactions destabilize polar order for both pushers and pullers, giving rise to rich collective spatiotemporal behaviors beyond the simple symmetry breaking of the dry Vicsek model. Pusher systems feature active turbulence with nonuniversal scaling exponents in the kinetic energy spectrum function, revealing a route toward active turbulence via self-steering. Pullers assemble in dense, swarming clusters driven by hydrodynamic interactions. Toroidal structures are observed in the vorticity field, which are characterized by enhanced spatial vorticity-velocity cross-correlations at short distances. This demonstrates that the formation of vortex rings is a direct consequence of strong active jets caused by propulsion and alignment.

II. HYDRODYNAMIC VICSEK MODEL AND POLAR ORDER

We consider a system of N spherical squirmers with radius R_{sq} and instantaneous orientation $\mathbf{e}_i$, $i \in \{1, \ldots, N\}$. Self-propulsion and self-steering is achieved via the surface-slip boundary condition

$$u_\theta = \frac{3}{2} v_0 \sin\theta (1 + \beta \cos\theta) - \frac{1}{R_{\mathrm{sq}}^2} (\tilde{C}_{11} \cos\phi - C_{11} \sin\phi), \tag{1}$$

$$u_\phi = \frac{\cos\theta}{R_{\mathrm{sq}}^2} (C_{11} \cos\phi + \tilde{C}_{11} \sin\phi), \tag{2}$$

where θ and ϕ are the polar and azimuthal angles in a body-fixed reference frame, see also Figs. 1(b) and 1(c). Self-propulsion by the axisymmetric components is characterized by the swim speed v_0 and the active stress β, where $\beta > 0$ for pullers and $\beta < 0$ for pushers [12,14,61]. Self-steering is modeled via the nonaxisymmetric surface-flow components C_{11} and $\tilde{C}_{11}$, which lead to a rotational motion of the body. These steering flows are designed to be of purely rotational nature such that a complete cancellation of the corresponding flow field is achieved (therefore called *stealth mode*) [52,57].

We render the nonaxisymmetric flow fields adaptive via the choice

$$C_{11} = C_0 R_{\mathrm{sq}}^3 (\mathbf{e} \times \mathbf{e}_{\mathrm{aim}}) \cdot \mathbf{e}_x, \tag{3}$$

$$\tilde{C}_{11} = C_0 R_{\mathrm{sq}}^3 (\mathbf{e} \times \mathbf{e}_{\mathrm{aim}}) \cdot \mathbf{e}_y, \tag{4}$$

with the unit vectors $\mathbf{e}_x$ and $\mathbf{e}_y$ perpendicular to the orientation vector $\mathbf{e}$ of the body-fixed reference frame, which enables the squirmer to reorient in the desired direction $\mathbf{e}_{\mathrm{aim},i}$ with the angular velocity [62]

$$\boldsymbol{\omega}_i = C_0 \mathbf{e}_i \times \mathbf{e}_{\mathrm{aim},i}, \tag{5}$$

where C_0 characterizes the strength of adaptation.

In Eq. (5), sensed information of each particle about the orientation of other neighboring particles is represented by a vector $\mathbf{e}_{\mathrm{aim},i}(\{\mathbf{e}_j\})$. In the interest of the investigation and understanding of the generic collective behavior of an active polar fluid, we focus here on a minimal model, where only the swimming and steering mechanism via the adaptive surface flow field is explicitly considered, whereas sensing and information processing is considered implicitly by the vector $\mathbf{e}_{\mathrm{aim}}$, see also Ref. [52]. As a representative example of assembled information between intelligent microswimmers, we consider a Vicsek-type alignment interaction, where each microswimmer aims at adapting its orientation and propulsion direction to the average orientation of neighboring particles,

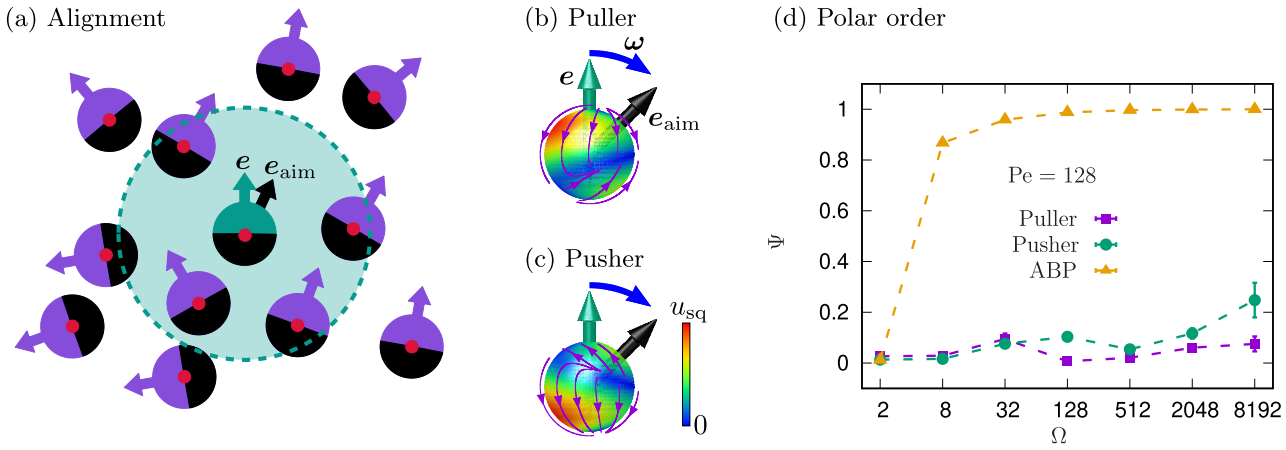

FIG. 1. Illustration of the alignment interaction. (a) The microswimmer with the orientation **e** (petrol) senses the orientations of neighboring microswimmers (purple) within the sensing range R_a (green dashed circle) and reorients toward $\mathbf{e}_{\rm aim}$ (black arrow), which is the average orientation of the neighbors determined via Eq. (6). Nonaxisymmetric surface flow fields for hydrodynamic self-steering of (b) puller-type and (c) pusher-type microswimmers with angular velocity $\boldsymbol{\omega}$. Adapted from Ref. [52]. (d) Global polar order parameters Ψ for pullers (purple squares), pushers (green circles), and active Brownian particles (yellow triangles) as a function of the maneuverability Ω for Pe = 128.

see Fig. 1(a) for illustration, where [63]

$$\mathbf{e}_{{\rm aim},i} = \frac{1}{N_i}\sum_{j\in\Gamma_i}\mathbf{e}_j. \tag{6}$$

Here, Γ_i is the set of neighbors of the ith particle in its alignment range R_a, and N_i is the number of neighbors. Note that, due to the normalization by the number of neighbors, Eq. (6) represents a nonadditive rule of orientation adaptation, which results in nonreciprocal interactions. As apparent from Eq. (6), $\mathbf{e}_{\rm aim}$, which serves as an input signal triggering adaptive surface flows according to Eqs. (1) and (2), is typically not a unit vector. Therefore, the magnitude of the adaptation torque depends on the orientational order of the neighboring microswimmers. We emphasize that, in our approach, the steering is achieved solely via the modification of the surface flow field, mimicking the autonomous behavior of microorganisms, in contrast with external driving forces, see, e.g., Ref. [64]. We also note that this distinguishes our model from ferromagnetic-type alignment or nematic interactions among elongated particles, as Stokeslets due to interparticle forces should not dominate the dynamics. This difference leads to very different behaviors in wet and dry systems.

For the fluid simulations, we consider a MPC variant with angular momentum conservation [65,66], see Appendix A for more details. For an accurate characterization of emergent behaviors, we consider large system sizes up to $L/a = 1024$, where L is the length of the cubic simulation box, and a is the side length of a MPC collision cell, and up to $N = 884\,736$ squirmers. The employed simulation code is highly parallelized and GPU-accelerated [67], enabling the consideration of large-scale systems to capture long-range hydrodynamics interactions and to minimize potential finite-size effects. For the squirmers, we choose the sensing range $R_a = 4R_{\rm sq}$ and strength of the active stress $\beta = -3$ and 3 for pushers and pullers, respectively. For example, the value $\beta = -3$ corresponds approximately to that of *E. coli* bacteria [20]. For most simulations, we consider the packing fraction $\rho \equiv (4\pi R_{\rm sq}^3/3)N/L^3 = 0.093$ (based on the squirmer radius) or $\rho_a \equiv (4\pi R_{\rm a}^3/3)N/L^3 \approx 6.0$ (based on sensing range), if not explicitly stated otherwise. Excluded-volume squirmer-squirmer interactions are modeled via the separate-shifted Lennard-Jones potential, see Appendix B. For comparison, we also perform simulations of a dry system of aligning self-steering intelligent active Brownian particles of the same packing fraction [62].

For the characterization of self-propulsion and self-steering, we introduce two dimensionless parameters, the Péclet number Pe and the maneuverability Ω, in the form

$$\mathrm{Pe} = \frac{v_0}{\sigma D_R}, \quad \Omega = \frac{C_0}{D_R}, \tag{7}$$

where $\sigma = 2R_{\rm sq}$ and D_R are the diameter and the (thermal) rotational diffusion coefficient of a squirmer, respectively. Explicitly, the values $v_0/\sqrt{k_{\rm B}T/m} = 0.007\,872$ and $0.031\,488$ are used, which correspond to Pe = 32 and 128, and the Reynolds numbers Re = 0.022 and 0.089. The values of the self-steering strength C_0 are varied from 0 to $0.335\,872\sqrt{k_{\rm B}T/m}/a$, which yields $0 \leqslant \Omega \leqslant 8192$. These maneuverability values are within the range of the estimated values from experiments on various microorganisms (bacteria, eukaryotes) and microbots, as provided in Appendix C, Table I, and Appendix D.

Results for the global polar order parameter $\Psi \equiv |\sum_i \mathbf{e}_i|/N$ are shown in Fig. 1(d). While dry and wet systems are disordered for a small maneuverability Ω, global polar order emerges only in dry systems for large Ω, indicating that hydrodynamic interactions destabilize the polar order. Instead of simple polar ordering, our squirmer systems show swarming dynamics with and without density modulation depending on the swimming mechanism (pusher or puller).

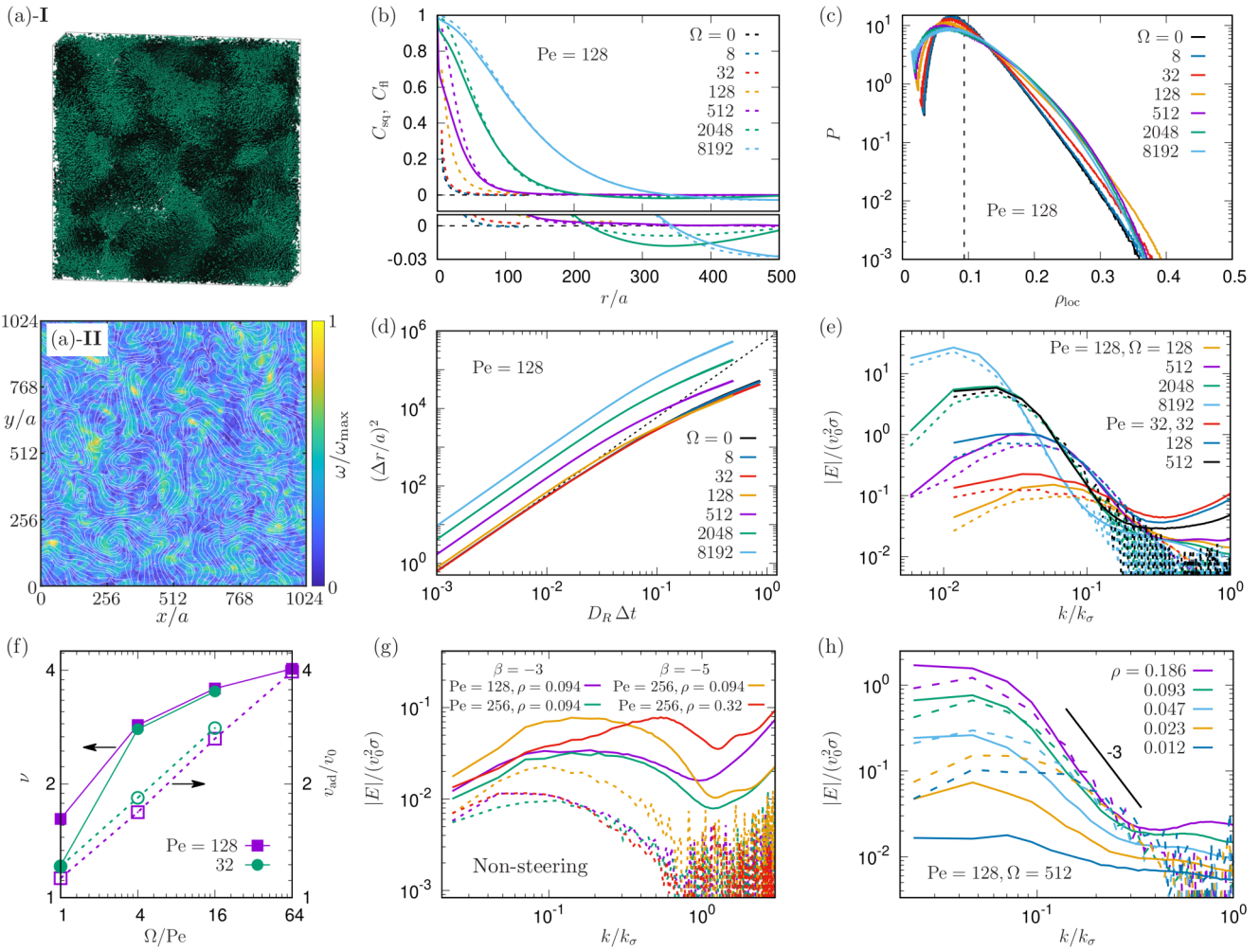

FIG. 2. Active turbulence in pusher systems. (a)-I Snapshot of squirmers for Pe = 128 and Ω = 2048. The orientation of each particle is indicated by a petrol hemisphere. (a)-II Two-dimensional projection of the streamlines of the velocity field (white lines) and the magnitude of the vorticity field (heat map) for Pe = 128 and Ω = 2048. (b) Equal-time spatial velocity correlation functions of squirmers C_{sq} (dashed) and fluid C_{fl} (solid) as a function of distance for various Ω, as indicated in the legend. An enlarged view for small correlations is shown in the bottom panel. (c) Squirmer density distribution as a function of the local packing fraction for various Ω's. The global packing fraction is represented by a black dashed line at $\rho_{loc} \approx 0.093$. (d) Mean-square displacement (MSD) as a function of time for various Ω's (legend). The black dashed line indicates the ballistic dynamics of noninteracting squirmers $(\Delta r)^2 = {v_0}^2(\Delta t)^2$, and D_R is the rotational diffusion coefficient. (e) Energy spectrum function for squirmers (dashed) and fluid (solid) as a function of the wave number k for Ω/Pe = 1, 4, 16, and 64, and Pe = 32 and 128. $k_\sigma = 2\pi/\sigma$ is the wave number for the squirmer diameter. (f) Advection speed v_{ad} [open symbols, extracted from the MSD data in (d)] and exponent ν of the energy spectrum function [filled symbols, obtained from (e)] as a function of Ω/Pe for Pe = 32 and 128. (g) Energy spectra of the fluid (solid) and the squirmers (dashed) as a function of the wave number for nonsteering microswimmers and the indicated parameter sets. (h) Energy spectra of the fluid (solid) and the self-steering squirmers (dashed) for various densities (legend) and Pe = 128, Ω = 512. In (g) and (h), $L/a = 256$.

III. PUSHERS: ACTIVE TURBULENCE VIA SELF-STEERING

Systems of squirmers propelled from the rear (pushers) exhibit active turbulence, see Fig. 2(a)-I for a snapshot (also Movie S1 in the Supplemental Material [68]), as is reflected in the presence of collective vortical flows and a power-law decay of the energy spectrum function [19–21]. Figure 2(a)-II illustrates the fluid velocity field with vortical structures and fluctuations in the magnitude of the vorticity. Accordingly, equal-time spatial squirmer velocity correlations C_{sq} become negative at large distances (less than $L/2$) for large Ω, see Fig. 2(b). The fluid spatial correlation function C_{fl} computed from the fluid velocity field $\mathbf{v}_{fl}$ exhibits a similar behavior (see Appendix E for detailed description of computing C_{sq} and C_{fl}). However, no pronounced density fluctuations are visible, see Fig. 2(a)-I. This is confirmed by the analysis of the local density distribution via Voronoi tessellation [69]. As shown in Fig. 2(c), the distribution exhibits a peak near the global squirmer density independent of Ω.

To characterize the dynamics, we examine the kinetic energy spectrum as a representative indicator of active turbulence [19,20]. We determine the energy spectra for both the squirmer and the fluid. For the squirmers, we first calculate spatial velocity correlation function and then perform a Fourier transform to obtain the energy spectrum. For the fluid,

we calculate the energy spectrum directly from the (Eulerian) velocity field. We refer to Appendix E for more details.

Before proceeding to a more detailed analysis of systems of self-steering squirmers, we briefly address the dynamics of pushers without self-steering, i.e., squirmers with $\Omega = 0$. Such systems exhibit no collective behavior independent of the Péclet number and the active stress up to high concentrations, as shown in Fig. 2(g), where no extended power-law regimes can be identified for $k < k_\sigma$ (see also Movie S2 in the Supplemental Material [68]). This is consistent with simulations of spherical squirmers confined in a narrow slit [66]. Here, flow-field interactions enhance the rotational diffusive motion of the squirmers, which can lead to short-lived clusters, but no collective motion appears. Collective motion emerges for elongated squirmers only [66]. These results are in line with theoretical studies on the stability of aligned and isotropic suspensions of self-propelled particles, which are always unstable to fluctuations [43,48]. In addition, nonlinear effects lead to strong density fluctuations, which result in an efficient fluid mixing [43].

In sharp contrast, systems of self-steering squirmers display pronounced self-organization, as demonstrated in Fig. 2. With increasing maneuverability Ω, a power-law regime emerges in the fluid energy spectrum for wave numbers $k/k_\sigma \lesssim 0.3$, see Fig. 2(e). Corresponding energy spectra of the squirmer motion exhibit the same behavior with the same exponents— extending even to smaller wave numbers $k/k_\sigma \approx 0.02$ for $\Omega = 8192$ as more squirmers participate in the self-organized vortex structures—confirming the emergence of active turbulence, where the dynamics of squirmers and fluid are strongly correlated on larger length scales. Fitting a power-law function $E(k) \sim (k/k_\sigma)^{-\nu}$ to this regime, we obtain maneuverability-dependent, nonuniversal exponents ν, roughly in the range $2.8 \lesssim \nu \lesssim 4.0$ for $4 \leqslant \Omega/\mathrm{Pe} \leqslant 64$, as presented in Fig. 2(f). We also note that the values obtained from $\mathrm{Pe} = 32$ and 128 agree well with each other in this regime.

Moreover, the peak height in the energy spectrum increases with increasing Ω, up to $|E| \approx 200 v_0^2 \sigma$ for $\Omega/\mathrm{Pe} = 64$. This indicates that squirmers attain much higher velocities, which is quantitatively confirmed by the squirmer mean-square displacement (MSD), see Fig. 2(d). In the ballistic regime, the MSD is given by $\langle (\Delta r)^2 \rangle = v_{\mathrm{ad}}^2 (\Delta t)^2$ with the advection speed v_{ad}. Hence, the increasing amplitude in Fig. 2(d) reflects the increasing speed as Ω increases for $\Omega \geqslant 512$, i.e., in the regime where a wide power-law region can be identified in the energy spectrum [Fig. 2(e)]. The Péclet number Pe merely affects the turbulent dynamics on large length scales, but the ratio Ω/Pe determines the exponent ν as well as the advection speed v_{ad}, as shown in Fig. 2(f).

The advection speed v_{ad} shows speedups up to a factor 4 in the self-steering system, as shown in Fig. 2(f). This agrees well with the experimental observation in bacterial turbulence with speedups up to a factor of 5 or 6 [21], whereas previous theoretical studies on nonsteering pushers have reported only up to a few tens of a percent increase in microswimmer speeds [70]. Moreover, in our system, speedups are achieved at a relatively low microswimmer density, comparable with the bacterial packing fractions of a few percent in experiments [71]. Our observation therefore implies that an additional factor other than self-propulsion and far-field hydrodynamics, like autonomous steering due to, e.g., oxygen-diffusion or buoyancy effects [28], may contribute to the emergence of *in vitro* bacterial turbulence in three dimensions.

We also probe density effects varying the number of squirmers. We first notice that the fluid energy spectra seem to converge for high densities, as shown in Fig. 2(h), in accordance with results of a previous noise-free Lattice Boltzmann study of dipole swimmers [72]. As the packing fraction ρ decreases from 0.186 to 0.012 corresponding to $\rho_a = 11.9$ and 0.768, a decrease of the fluid energy spectrum is observed, indicating that fluid stirring by squirmers is weak at low densities. Consequently, the apparent power-law regime in the energy spectrum of squirmers decreases with decreasing density and vanishes at about $\rho = 0.01$.

For $k/k_\sigma \gtrsim 0.5$, or length scales smaller than about 2σ, differences between the fluid and squirmer energy spectra appear. In this regime, near-field hydrodynamic flows play a significant role. Moreover, the properties of the energy spectra depend on Pe, indicating that noise effects are significant at these small length scales, see Appendix F for thermal fluid energy spectra [73]. Therefore, in wet systems and small densities, a strong self-steering of active particles is crucial for the emergence of a large-scale coherent collective motion. Otherwise, disorder and hydrodynamic instabilities on small length scales may prevail [48]. Such an observation should also apply to systems where alignment is mediated via steric repulsion of elongated body shapes [20] or strong hydrodynamic force dipoles [72]. In any case, in active turbulence of wet systems, collective fluid flows induced by microswimmers imply the collective behavior of microswimmers on large length scales with fast dynamics.

In contrast, active turbulence in dry systems of spherical objects [74] requires densely packed active particles and, e.g., a polydispersity, to prevent MIPS, because a speedup mechanism as in wet systems is lacking, as steric repulsion may only result in a slowdown of active particles. Hence, in dry active turbulence, a power-law regime develops at large k values or, equivalently, in small $|E|$ regimes due to chaotic interparticle collisions on small length scales.

IV. PULLERS: SWARMING DYNAMICS VIA SELF-STEERING

In systems of self-steering pullers, a rich swarming dynamics develops, as shown in Fig. 3. The self-organization is characterized by the formation of morphologically complex clusters of microswimmers which, on larger length scales, exhibit visually chaotic movements and exchange squirmers with each other, see Fig. 3(a)-I (also Movie S3 in the Supplemental Material [68]). Still, the puller system exhibits a velocity field with vortical structures [see Fig. 3(a)-II], surprisingly similar to pushers.

A. Density modulation

The local density distribution is calculated via Voronoi tessellation [69]. In sharp contrast with pusher systems [Fig. 2(c)], puller systems exhibit significant density modulations, see Fig. 3(b). For large $\Omega \gtrsim 4096$, the density

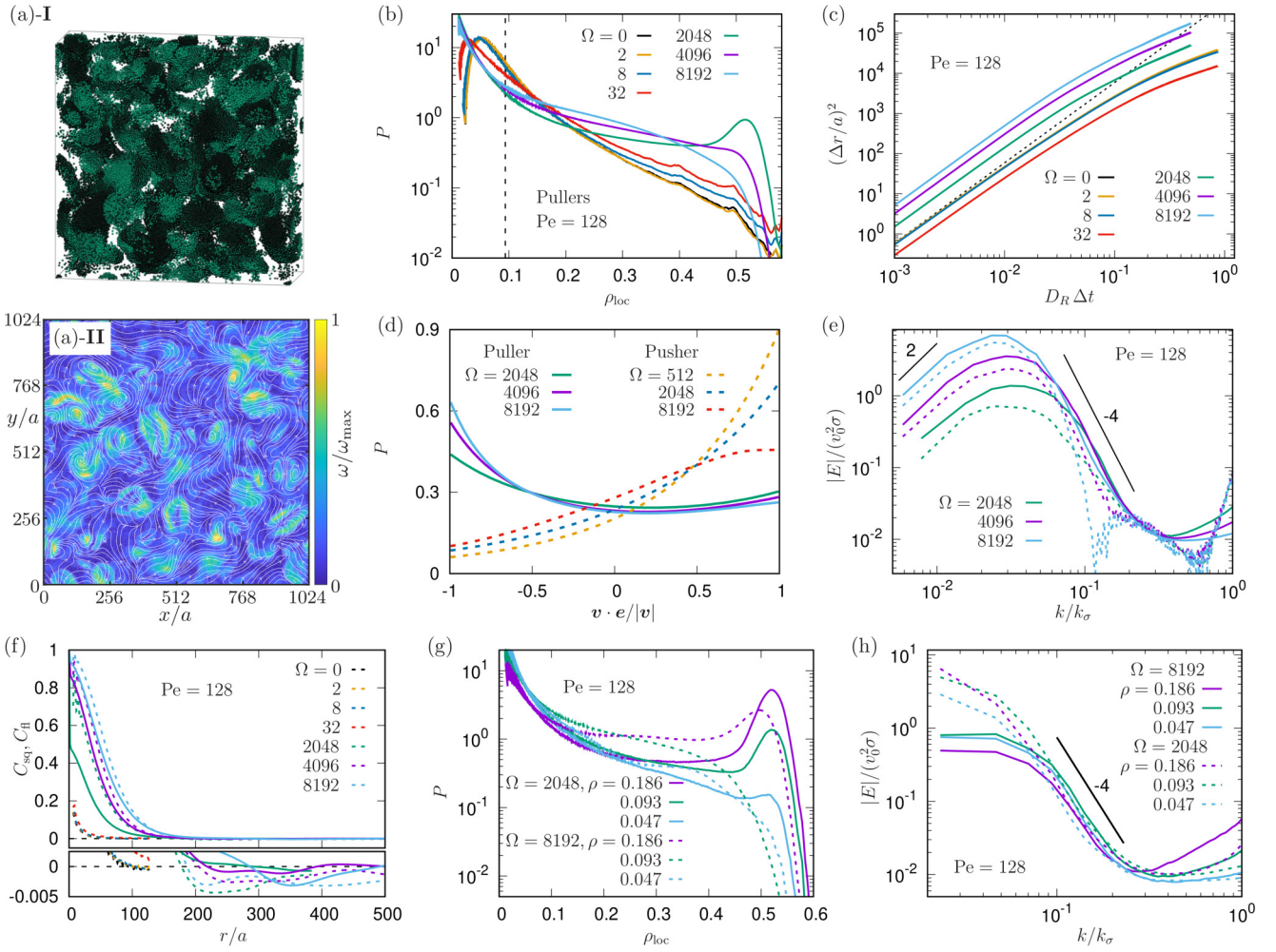

FIG. 3. Swarming dynamics in puller systems. (a)-I Snapshot of squirmers with their orientation indicated by a petrol hemisphere. (a)-II Two-dimensional projection of the streamlines of the velocity field (white lines) and the magnitude of the vorticity field (heat map) for Pe = 128 and $\Omega = 8192$. (b) Squirmer density distribution as a function of the local packing fraction for various Ω's. The global packing fraction is represented by a black dashed line at $\rho_{\rm loc} \approx 0.093$. (c) Mean-square displacement as a function of time for various Ω's (legend). The black dashed line indicates the ballistic dynamics of noninteracting squirmers $(\Delta r)^2 = v_0^2(\Delta t)^2$. (d) Distribution function of the product $\mathbf{e}\cdot\mathbf{v}/|\mathbf{v}|$ of the orientation and velocity vector for pullers (solid lines) and pushers (dashed line). (e) Energy spectra for squirmers (dashed) and fluid (solid) as a function of the wave number k for various Ω's (legend). The short black lines represent power laws with the exponents 2 and -4 as guides for the eye. (f) Equal-time spatial correlation functions for squirmers $C_{\rm sq}$ (dashed) and fluid $C_{\rm fl}$ (solid). An enlarged view for small correlations is shown in the bottom panel. (g) Local density distribution and (h) energy spectrum of the fluid as a function of the wave number, for Pe = 128, $\Omega = 2048$ (dashed), and $\Omega = 8192$ (solid) at various densities, as indicated.

distribution is broad, while for $\Omega = 2048$, a clear tendency of segregation is observed (Movie S4 in the Supplemental Material [68]), with a low-density peak at $\rho_{\rm loc} \approx 0$ and a high-density peak at $\rho_{\rm loc} \approx 0.5$. For small Ω in the range $128 \leqslant \Omega \leqslant 512$, nonmobile clusters appear, see Appendix G. We focus here on the dynamic clusters, as formation of a dense static cluster may be affected by a depletion of MPC fluid particles inside the cluster, which is related to the (weak) compressibility of the MPC fluid, and artificially enhances cluster stability [66]. For $\Omega \leqslant 32$, unimodal distributions are recovered but with a peak at a density smaller than the global density of $\rho = 0.093$ and with fatter tails than those in pusher systems, which reflects the clustering tendency reported for pullers [34,66].

B. Decoupling of puller orientation and velocity

The emergence of a high-density regime for $\Omega \geqslant 2048$ needs to be distinguished from MIPS in dry systems. First, squirmers in a (small) cluster exhibit local polar order, giving rise to a coherent directional motion of the cluster. Second, the pullers swim faster on average than their bare self-propulsion speed v_0, as shown in Fig. 3(c), as in the system of pushers [see Figs. 2(d) and 2(f)]. Decoupling of self-propulsion and velocity of squirmers is far more significant than in MIPS. Even situations where pullers are driven backward occur frequently (Movie S5 in the Supplemental Material [68]). Indeed, as shown in Fig. 3(d), the probability that the velocity of a squirmer is antiparallel to its orientation, i.e., $\mathbf{v}/|\mathbf{v}| = -\mathbf{e}$, is even higher than that for the parallel case,

i.e., $\mathbf{v}/|\mathbf{v}| = \mathbf{e}$. Therefore, we conclude that hydrodynamic interactions between self-steering pullers dominate over the self-propulsion forces. The attractive hydrodynamic interactions between aligned pullers in a head-to-tail configuration promote the formation of dense clusters. However, as we will demonstrate below, dense clusters are not static but exhibit a highly dynamical morphology.

C. Decoupling of puller and fluid dynamics

The kinetic energy spectra $E(k)$ for squirmer motion and the fluid in the puller systems are presented in Fig. 3(e). While for the swarming of pullers, $E(k)$ of the fluid exhibits a power-law decay in the intermediate wave-number regime ($0.04 < k/k_\sigma < 0.2$), as in pusher systems, several features significantly deviate from those of pushers, which again demonstrates the uniqueness of puller swarming. Above all, the energy spectrum of the squirmers shows no universality in the range $0.03 < k/k_\sigma < 0.1$, in contrast with the MPC fluid. Moreover, a pronounced mismatch between the squirmer and fluid energy spectra is observed in the vicinity of $k/k_\sigma \approx 0.1$, which indicates that pullers are not simply driven by the fluid flow, but in addition, inter-squirmer interactions are important. This is reflected in the squirmer spatial velocity correlation function C_{sq} in Fig. 3(f), which exhibits oscillations for small r/a at large Ω, in contrast with those of pushers [Fig. 2(b)]. In addition, pullers exhibit much smaller negative values in the spatial correlation functions for large r/a than those of pushers.

The power-law behavior of the fluid for the intermediate regime ($0.04 < k/k_\sigma < 0.2$) even persists under variation of global densities. By varying the number of pullers, the density dependence of the energy spectrum is analyzed for the relatively small system size of $L/a = 256$. As the kinetic energy spectrum of squirmers is significantly impaired for small system sizes (see Appendix H), only the fluid energy spectrum is considered. As shown in Fig. 3(h), the puller density affects the energy spectrum only weakly. The estimated exponent for $0.1 < k/k_\sigma < 0.2$ is $\nu \approx 4$, in agreement with Fig. 3(e). However, the global puller density significantly alters the local squirmer density distribution, as shown in Fig. 3(g). As the squirmer density decreases, a shift of the high-density peak to lower densities is observed, which then may disappear completely at low densities.

D. Formation of vortex ring

An even more striking feature is observed in configurations of the vorticity field. Visual observation of the time evolution of the system indicates a typical dynamical behavior in the morphology of clusters, which involves the pulsatile transformation of aggregates from a spherical shape into jellyfish-like arrangements. In terms of fluid mechanics, the jellyfish-like morphology suggests formation of a vortex ring, which is indeed confirmed by the emergence of toroidal structures in the vorticity fields extracted from the simulations, see Fig. 4(a). As shown in Fig. 4(b), the vorticity field exhibits whirling patterns within regions where the magnitude of the vorticity field is large.

For a detailed illustration, we consider the small system size $L/a = 128$, where only a single cluster emerges (Movie S6 in the Supplemental Material [68]). As shown in Fig. 4(c)-I, the dynamics initiates with formation of a cluster. Then due to alignment, squirmers rotate, and a polar order emerges within the cluster, see Fig. 4(c)-II, and Fig. 4(d) for the corresponding order parameter. Such an ordered structure gives rise to a strong collective fluid flow, which generates a pronounced jet in front of the cluster, see the yellow surface in Fig. 4(f)-I. Notably, the jet flow is self-generated via active stirring of microswimmers in this case, instead of an external perturbation as in passive hydrodynamic fluids. Subsequently, a spread-out motion of squirmers is initiated [Fig. 4(c)-III]. Simultaneously, a vortex ring is formed around the cluster [blue ring in Fig. 4(f)-I], while squirmers are moving forward. As shown in Fig. 4(e), the velocity field is indeed wrapping around the vortex ring, in accordance with Fig. 4(b). Then the pullers continue to spread out, rolling about the region where the vortex ring forms, see Fig. 4(c)-IV. While swimmers at the cluster center swim forward, they are dragged backward at the periphery, as shown in Fig. 4(f)-II, which contributes to the anomalous behavior in the distribution function of $\mathbf{v} \cdot \mathbf{e}/|\mathbf{v}|$ [see Fig. 3(d)]. Eventually, the cluster dissolves, ending its life cycle.

To examine potential inertia effects, we further determine a cluster Reynolds number Re_c of dynamic clusters by extracting collective advection speeds from the MSD data [Fig. 3(c)] and cluster sizes from the squirmer spatial correlation functions [Fig. 3(f)]. For the latter, we use the distance of the first intercept, where C_{sq} decays to zero for the first time. We then obtain $\mathrm{Re}_c = 4.19$, 7.03, and 8.13 for $\Omega = 2048$, 4096, and 8192, respectively. Not surprisingly, these values are significantly larger than the particle Reynolds numbers. However, the Re_c values between 1 and 10 still remain within the laminar hydrodynamic regime, which clearly indicates that the observed chaotic behavior does not arise from inertial effects.

V. VELOCITY-VORTICITY COUPLING

The sequential time evolution described so far indicates a strong coupling between the fluid velocity and the vorticity field in a puller cluster. As shown in Fig. 5(a), the rotation of the velocity field for pullers is indeed centered at regions with a strong velocity field.

For a more quantitative characterization, we examine the distribution of the Cartesian components of the velocity and vorticity fields. Specifically, we examine the squirmer velocity and vorticity distribution, $\bar{v}_\alpha$ and $\bar{\omega}_\alpha$, respectively, along an axis of the Cartesian reference frame (e.g., v_α for $\alpha = x, y, z$), averaged over all three components for both pushers and pullers and various Ω. In pusher systems, both the velocity and vorticity fields [Figs. 5(b) and 5(c)] exhibit a Gaussian distribution, which is an indicator of active turbulence [20]. For pullers, both deviate from a Gaussian, demonstrating that the swarming dynamics of pullers is not active turbulence. Specifically, the velocity distribution of pullers exhibits fat exponential tails, as shown in Fig. 5(b), in line with the emergence of stronger fluid flows than expected, i.e., the occurrence of jet plumes induced by aligned pullers. Also the distribution of the vorticity field for pullers is broader than that of pushers, as displayed in Fig. 5(b).

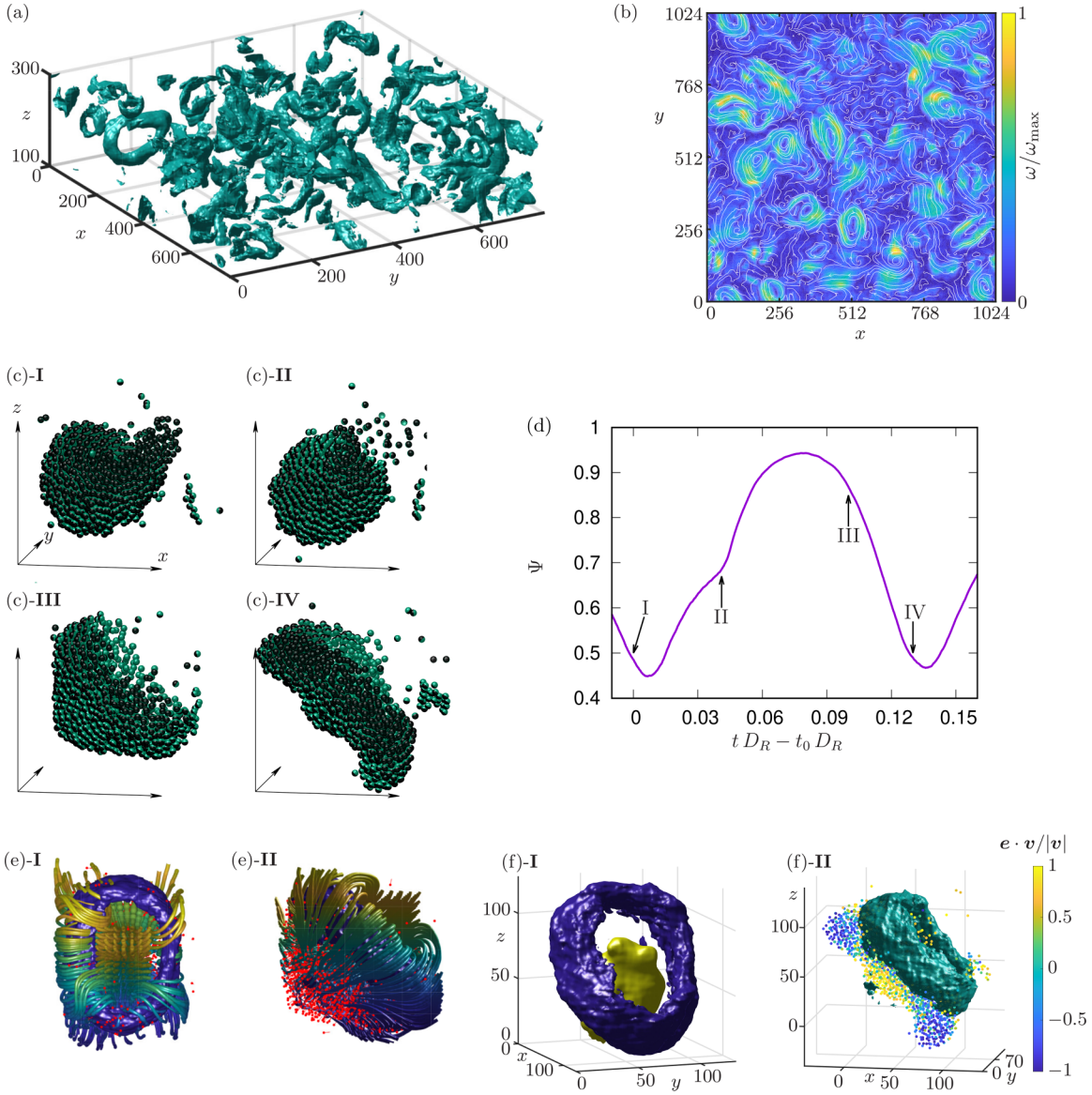

FIG. 4. Formation of vortex rings. (a) System cutout ($100 \leqslant z/a \leqslant 300$) of the surface plot for the vorticity field with Pe $= 128$, $\Omega = 2048$, $L/a = 768$, and $\omega \approx 0.33\omega_{\max}$, where $\omega_{\max}$ indicates the maximum value of ω in the system at this time step. (b) Quasi-two-dimensional slice of the vorticity field, projected onto the corresponding two dimensions (white lines), together with the magnitude of the vorticity field (heat map) for Pe $= 128$, $\Omega = 8192$, and $L/a = 1024$. (c) Time evolution of a squirmer configuration during the emergence and destruction of a vortex ring for I $t = t_0$ (formation of cluster), II $t_1 = t_0 + 0.041/D_R$ (formation of jet flow), III $t_2 = t_0 + 0.10/D_R$ (emergence of vortex ring), and IV $t_3 = t_0 + 0.13/D_R$ (jellyfishlike spreading of squirmers). (d) Time evolution of the global order parameter Ψ for the cluster in (c). The data points corresponding to the snapshots are indicated by arrows with the indices I–IV. (e) Vortex ring (blue torus, $\omega \approx 0.4\omega_{\max}$) and fluid velocity field (tubes) together with the squirmer positions (red bullets) and orientations (indicated by red bars) at $t = t_2$. I Top view and II side view of the vortex ring, which depicts the cluster of squirmers shown in (c)-III pulling fluid on the top right toward the cluster. Squirmers in the frontal region of the cluster are moving along the outer surface of the vortex ring, see also (c)-III to identify the locations of the vortex ring and squirmers. (f)-I Surface plot of the jet flow ($|\mathbf{v}_{\text{fl}}| \approx 1.6v_0$) generated at $t = t_1$, together with the vortex ring subsequently formed at $t = t_2$. Note that the jet flow is formed at the frontal region of the aligned cluster [see (c)-II] and directed toward the cluster. (f)-II Positions and velocities of the squirmers (bullets) at $t = t_3$ [see (c)-IV], together with the vortex ring previously formed at $t = t_2$. The colors of the squirmers indicate the product $\mathbf{e} \cdot \mathbf{v}/|\mathbf{v}|$ of their orientation and swim direction. In (c)–(f), Pe $= 128$ and $\Omega = 2048$.

Furthermore, the distribution function of the average of the three Cartesian components of the vorticity $\boldsymbol{\omega}$, ω_α ($\alpha = x, y, z$), Fig. 5(c), shows a rather narrow peak, indicating a weak separation between regions with strong and weak vorticity.

A more fundamental difference in the velocity-vorticity coupling is revealed by the cross-correlations between the magnitude of vorticity and that of the velocity field ($|\boldsymbol{\omega}(\mathbf{r})|$ and $|\mathbf{v}(\mathbf{r})|$), as defined in Appendix E. In Fig. 6, the various cross-correlations for pushers exhibit a pronounced peak at

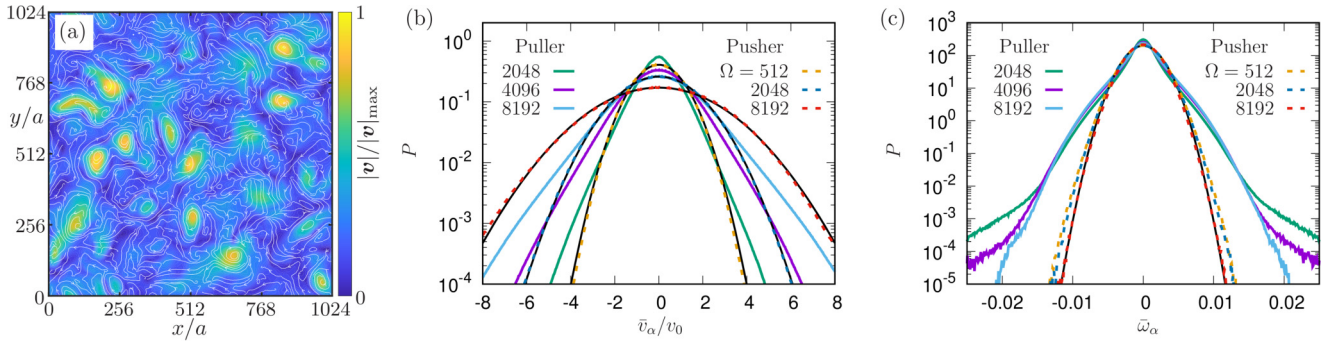

FIG. 5. Velocity-vorticity coupling. (a) Vorticity field of pullers (white lines) combined with the magnitude of the velocity field [heat map; see Fig. 4(b)]. (b) Distribution of the Cartesian squirmer velocity component $\bar{v}_\alpha$, averaged over the three coordinate directions, for pushers (solid) and pullers (dashed) with the indicated maneuverability values. (c) Distribution of the Cartesian components of the vorticity field $\bar{\omega}_\alpha$ as a function of the vorticity ω. In (b) and (c), black solid lines shows the Gaussian distribution. Here, Pe = 128.

$r/a = 20$, 60, and 120 for $\Omega = 512$, 2048, and 8192, respectively, while the cross-correlation at $r = 0$ is not strong. Hence, for pushers, the velocity field of a vortex is weak at the center but strong at intermediate regions between the center and periphery. In sharp contrast, for pullers, the cross-correlation between the vorticity and the velocity field is already strong at small distances. This demonstrates that a strong velocity field generates a strong vorticity in the immediate vicinity of the jet flow. Moreover, the cross-correlation decays faster than for pushers, assuming negative values before approaching zero.

VI. DISCUSSION AND CONCLUSIONS

We have studied the self-organization and dynamics in three-dimensional wet systems of self-steering squirmers, which aim for alignment of their orientation with their neighbors. We demonstrate that alignment via hydrodynamic self-steering gives rise to rich collective behavior in such polar active fluids, depending on the type of active stress, i.e., whether the microswimmers are pushers or pullers. In both cases, an essential role of hydrodynamics is the breaking of long-range polar order, which causes the emergence of a chaotic motion.

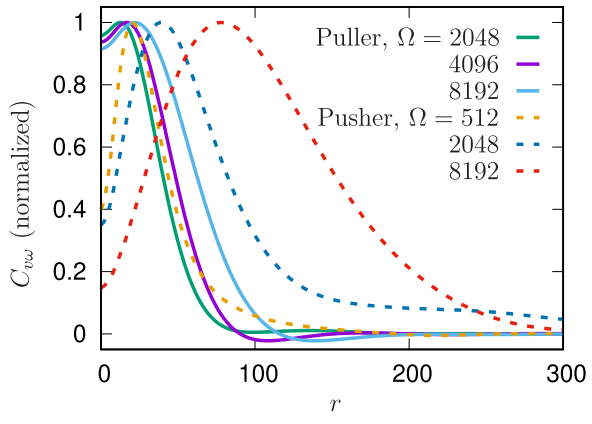

FIG. 6. Velocity-vorticity cross-correlation. Cross-correlation function between the velocity and the vorticity field as a function of the radial squirmer distance for various maneuverabilities and Pe = 128.

For pushers, the particle distribution is quite homogeneous for the considered densities, the distribution of the Cartesian velocity components is Gaussian, and the kinetic energy spectrum displays a peak and a subsequent power-law decay with increasing wave vector, which indicates active-turbulent behavior. An intriguing feature is that strong self-steering enhances the locally coherent movement of microswimmers, which leads to local fluid flows with speeds much faster than the individual swim speed, as is reflected in the increasing magnitude of the peak in the energy spectrum combined with an extension of the scaling regime toward large length scales, as well as an amplification of the MSD. This implies that large-scale flows are induced by the collective motion, which drag the microswimmers along and supersede their individual motion. Thus, the polarity field and the fluid flow field are strongly coupled.

For pullers, another type of self-organization emerges, which is strictly distinguished from MIPS of dry active Brownian particle systems as well as active turbulence of pushers. Their density distribution is inhomogeneous, as the pullers tend to form clusters. However, these clusters are not static but tend to be unstable and dynamic. The particle alignment inside the cluster generates a strong fluid jet and a vortex ring, which pulls apart the cluster and leads to its disintegration. These strong flows imply that the probability of fast fluid flows is enhanced, which is reflected in the emergence of fat tails in the velocity distribution.

We like to emphasize that wet systems of self-propelled squirmers without self-steering are found in our simulations to display no interesting collective behavior in three dimensions, not even at high squirmer volume fractions. In contrast, lattice-Boltzmann simulations (without hydrodynamic fluctuations) of extended force dipoles with far-field hydrodynamic interactions and run-and-tumble motion have predicted active turbulence at high swimmer densities, where the fluid velocities are only slightly enhanced (roughly by a factor 2–3) compared with the swimming velocity of individual particles [72]. Results of lattice-Boltzmann simulations of (non-self-steering) squirmers have been interpreted as evidence for active turbulence, but the calculated energy spectrum functions display only a very narrow power-law regime [75].

Our numerical observations for ensembles of self-steering pullers challenges current theoretical views on collective behaviors in wet active systems. So far, it has been typically assumed that the polarity and velocity fields of active fluids are essentially identical, based on the assumption of a nearly homogeneous distribution of active particles. Heterogeneous densities have been observed recently in models of compressible polar active fluids for bacterial suspensions [76,77]; however, the mechanism is entirely different in this case, as hydrodynamic interactions are not considered, and clustering is driven by a strong dependence of self-propulsion speed on the local density.

Our results demonstrate that—in wet systems of self-steering microswimmers in three dimensions—the interplay of the particle density and polarity and of the fluid velocity field can give rise to a surprisingly rich variety of emergent behaviors already for highly simplified model systems with only a single particle type.

ACKNOWLEDGMENTS

The authors gratefully acknowledge the Gauss Centre for Supercomputing e.V. [78] for funding this project by providing computing time through the John von Neumann Institute for Computing (NIC) on the GCS Supercomputer JUWELS [79] at Jülich Supercomputing Centre (JSC).

DATA AVAILABILITY

The data that support the findings of this paper are openly available [80].

APPENDIX A: MESOSCALE FLUID MODEL: MPC

We adopt the MPC method [59,60], a particle-based mesoscale simulation approach, as the model for the fluid. Specifically, we employ the stochastic rotation variant of MPC [58,60] with angular momentum conservation (MPC − SRD + a) [65,82] and the cell-level Maxwell-Boltzmann scaling thermostat [83].

1. Fluid dynamics

A MPC fluid consists of N point particles of mass m, whose dynamics proceeds in alternating streaming and collision steps [59,60]. In the streaming step, the particles move ballistically according to

$$\mathbf{r}_i(t+h) = \mathbf{r}_i(t) + h\mathbf{v}_i, \tag{A1}$$

where $\mathbf{r}_i$ and $\mathbf{v}_i$ $(i = 1, \ldots, N)$ denote the positions and the velocities of the MPC particles, and the collision time h is the time interval between collisions. Coarse-grained interactions between MPC particles are modeled by a momentum conserving, stochastic process in the collision step, for which the whole system is divided into cubic collision cells of side length a, containing $\langle N_c \rangle$ MPC particles on average. These cells are randomly shifted to ensure Galilean invariance [84]. In MPC − SRD + a, the velocities after a collision are given by

$$\mathbf{v}_i(t+h) = \mathbf{v}_{\rm cm}(t) + \mathbf{D}(\alpha_c)\,\mathbf{v}_{i,c} + \boldsymbol{\omega}_c(t) \times \mathbf{r}_{i,c}(t). \tag{A2}$$

Here, $\mathbf{r}_{i,c} = \mathbf{r}_i - \mathbf{r}_{\rm cm}$ and $\mathbf{v}_{i,c} = \mathbf{v}_i - \mathbf{v}_{\rm cm}$ are the positions and velocities with respect to the center-of-mass position $\mathbf{r}_{\rm cm} = \sum_{i=1}^{N_c} \mathbf{r}_i/N_c$ and the center-of-mass velocity $\mathbf{v}_{\rm cm} = \sum_{i=1}^{N_c} \mathbf{v}_i/N_c$. The angular velocity is given by

$$\boldsymbol{\omega}_c = m\mathbf{I}_c^{-1} \sum_{i=1}^{N_c} \{\, \mathbf{r}_{i,c} \times [\mathbf{v}_{i,c} - \mathbf{D}(\alpha_c)\, _{i,c}]\}, \tag{A3}$$

where $\mathbf{D}(\alpha_c)$ denotes the rotation matrix for a rotation by an angle α_c around a randomly orientated axis of a collision cell, and $\mathbf{I}_c$ is the moment-of-inertia tensor of the MPC particles in the collision cell. A constant local temperature is maintained by a cell-level canonical thermostat (Maxwell-Boltzmann scaling thermostat) [83,85]).

2. Squirmer dynamics

a. Rigid body dynamics

A squirmer is consider as a spherical rigid body with translational and rotational degrees of freedom [56]. Newton's equations of motion for the translational motion are solved by the velocity-Verlet algorithm, which yields

$$\mathbf{r}(t+\Delta t) = \mathbf{r}(t) + \mathbf{u}(t)\Delta t + \frac{\Delta t^2}{2M}\mathbf{F}(t), \tag{A4}$$

$$\mathbf{u}(t+\Delta t) = \mathbf{u}(t) + \frac{\Delta t}{2M}[\mathbf{F}(t) + \mathbf{F}(t+\Delta t)], \tag{A5}$$

for the center-of-mass position $\mathbf{r}$ and velocity $\mathbf{v}$ of the squirmers, with the force $\mathbf{F}$ between squirmers, e.g., by the Lennard-Jones potential Eq. (B1), and the time step $\Delta t = h$, with $h = 0.02\, a\sqrt{m/(k_B T)}$.

The equations of motion of the rotational dynamics are solved via quaternions $\mathbf{q} = (q_0, q_1, q_2, q_3)^T$ [56,86,87]. In the body fixed reference frame, the equations of motion are

$$\dot{\mathbf{q}} = \frac{1}{2}\mathbf{Q}(\mathbf{q})\begin{pmatrix} 0 \\ \boldsymbol{\Omega}^{\rm b} \end{pmatrix}, \tag{A6}$$

$$\ddot{\mathbf{q}} = \frac{1}{2}\mathbf{Q}(\dot{\mathbf{q}})\begin{pmatrix} 0 \\ \boldsymbol{\Omega}^{\rm b} \end{pmatrix} + \frac{1}{2}\mathbf{Q}(\dot{\mathbf{q}})\begin{pmatrix} 0 \\ \dot{\boldsymbol{\Omega}}^{\rm b} \end{pmatrix}, \tag{A7}$$

with the matrix

$$\mathbf{Q}(\mathbf{q}) = \begin{pmatrix} q_0 & -q_1 & -q_2 & -q_3 \\ q_1 & q_0 & -q_3 & q_2 \\ q_2 & q_3 & q_0 & -q_1 \\ q_3 & -q_2 & q_1 & q_0 \end{pmatrix}, \tag{A8}$$

the angular velocity $\boldsymbol{\Omega}^{\rm b}$ in the body fixed frame, and its equations of motion in Cartesian coordinates $\alpha \in \{x, y, z\}$,

$$\frac{d\Omega_\alpha^{\rm b}}{dt} = I_\alpha^{-1}\left[T_\alpha^{\rm b} + (I_\beta - I_\gamma)\Omega_\beta^{\rm b}\Omega_\gamma^{\rm b}\right]. \tag{A9}$$

Here, $\mathbf{T}$ is the torque on the sphere and $\mathbf{I}$ its moment of inertia tensor. The equations in Eq. (A9) are Euler's equations of the rigid body dynamics and hold for $(\alpha, \beta, \gamma) = (x, y, z)$, (y, z, x), and (z, x, y). The steric interactions between the squirmers do not exert any torque. Hence, $d\boldsymbol{\Omega}^{\rm b}(t)/dt = 0$ for the homogeneous sphere and its inertia tensor is diagonal, i.e., $I_x = I_y = I_x = 2MR_{\rm sq}/5$. Equations (A6) and (A7) are solved by the Taylor expansion

$$\mathbf{q}(t+\Delta t) = (1-\tilde{\lambda})\mathbf{q}(t) + \dot{\mathbf{q}}(t)\Delta t + \frac{\Delta t^2}{2}\ddot{\mathbf{q}}(t), \tag{A10}$$

where the Lagrange multiplier $\tilde{\lambda}$ ensures the constraint $\mathbf{q}^2 = 1$ and is given by

$$\tilde{\lambda} = 1 - \dot{\mathbf{q}}^2\Delta t^2/2 - \sqrt{1 - \dot{\mathbf{q}}^2\Delta t^2 - \dot{\mathbf{q}}\cdot\ddot{\mathbf{q}}\Delta t^3 - (\ddot{\mathbf{q}}^2 - \dot{\mathbf{q}}^4)\Delta t^4/4}. \quad \text{(A11)}$$

and the angular momentum of the sphere $\mathbf{L}^{\mathrm{s}}$.

b. Squirmer-MPC fluid coupling

Coupling between the sphere and the MPC fluid occurs during the streaming and collision step, with a linear and angular momentum transfer. During the streaming step, a sphere collides with various MPC particles. Since the total change in (angular) momentum of a sphere during one streaming step is small, its collisions with MPC particles are perform in a coarse-grained manner [56,88]. For the streaming step at time t, the position, velocity, orientation, and angular velocity of the sphere at time $t + h$ are determined under the assumption that there is no interaction with MPC particles but potentially with other squirmers. Subsequently, all MPC particles are streamed, i.e., their positions are updated according to Eq. (A1), where a certain fraction of MPC particles penetrates the sphere. These particles are identified, translated onto the surface of the sphere, and the momentum transfer

$$\mathbf{J}_i^{\mathrm{str}} = 2m\{\mathbf{v}_i - \mathbf{u} - \boldsymbol{\Omega}\times(\mathbf{r}_i - \mathbf{r}) - \mathbf{D}^T\mathbf{u}_{\mathrm{sq}}^{\mathrm{b}}[\mathbf{D}(\mathbf{r}_i - \mathbf{r})]\} \quad \text{(A15)}$$

is determined by applying the bounce-back rule together with the squirmer surface fluid velocity $\mathbf{u}_{\mathrm{sq}}^{\mathrm{b}}$. The fluid velocities are correspondingly updated according to

$$\mathbf{v}_i' = \mathbf{v}_i - \mathbf{J}_i^{\mathrm{str}}/m. \quad \text{(A16)}$$

As a consequence of the elastic no-slip collisions, the center-of-mass velocity and rotation frequency of a colloid are finally given by

$$\mathbf{u}(t+h)' = \mathbf{u}(t+h) + \mathbf{J}/M, \quad \text{(A17)}$$

$$\boldsymbol{\Omega}(t+h)' = \boldsymbol{\Omega}(t+h) + \mathbf{D}^T(\mathbf{I}^{\mathrm{b}})^{-1}\mathbf{D}\mathbf{L}, \quad \text{(A18)}$$

where $\mathbf{J} = \sum_i \mathbf{J}_i$ is the total momentum transfer by the MPC fluid, and $\mathbf{L} = \sum_i[\mathbf{r}_i(t+h) - \mathbf{r}(t+h)]\times\mathbf{J}_i$ is the respective angular momentum transfer.

In the collision step, phantom particles are uniformly distributed inside a sphere, with the same mass and density as the fluid particles [84,88]. Their velocities are given by [56]

$$\mathbf{v}_i^{\mathrm{p}} = \mathbf{u} + \boldsymbol{\Omega}\times(\mathbf{r}_i - \mathbf{r}) + \mathbf{u}_{\mathrm{sq}}(\mathbf{r}_i) + \mathbf{v}_{\mathrm{R},i}, \quad \text{(A19)}$$

where the $\mathbf{v}_{\mathrm{R},i}$ are Gaussian-distributed random numbers with zero mean and variance $\sqrt{k_{\mathrm{B}}T/m}$. The surface slip velocity $\mathbf{u}_{\mathrm{sq}}(\mathbf{r}_i)$ is determined by Eqs. (1) and (2), with the phantom particle position $\mathbf{r}_i$ projecting onto the surface of the sphere. As a result of MPC collisions, the linear and angular momentum of a sphere change by $\mathbf{J}_i^{\mathrm{p}} = m(\mathbf{v}'^{\mathrm{p}}_i - \mathbf{v}_i^{\mathrm{p}})$ and $\mathbf{L}_i^{\mathrm{p}} = (\mathbf{r}_i^{\mathrm{p}} - \mathbf{r})\times\mathbf{J}_i^{\mathrm{p}}$, where $\mathbf{v}'^{\mathrm{p}}_i$ and $\mathbf{v}_i^{p}$ are the velocities of the phantom particles after and before the MPC collision. Hence, the colloid translational and angular velocity become

$$\mathbf{u}' = \mathbf{u} + \mathbf{J}^{\mathrm{p}}/M, \quad \text{(A20)}$$

$$\boldsymbol{\Omega}' = \boldsymbol{\Omega} + \mathbf{D}^T(\mathbf{I}^{\mathrm{b}})^{-1}\mathbf{D}\mathbf{L}^{\mathrm{b}}. \quad \text{(A21)}$$

The translational $\mathbf{v}^{\mathrm{s}}$ and angular velocity $\boldsymbol{\Omega}^{\mathrm{s}}$ in the laboratory frame follow from the relations

$$\mathbf{v}^{\mathrm{s}} = \mathbf{D}^T\mathbf{v}^{\mathrm{b}}, \quad \text{(A12)}$$

$$\boldsymbol{\Omega}^{\mathrm{s}} = \mathbf{D}^T(\mathbf{I}^{\mathrm{b}})^{-1}\mathbf{D}\mathbf{L}^{\mathrm{s}}, \quad \text{(A13)}$$

with

$$\mathbf{D} = \begin{bmatrix} q_0^2 + q_1^2 - q_2^2 - q_3^2 & 2(q_1q_2 + q_0q_3) & 2(q_1q_3 - q_0q_2) \\ 2(q_1q_2 - q_0q_3) & q_0^2 - q_1^2 + q_2^2 - q_3^2 & 2(q_2q_3 + q_0q_1) \\ 2(q_1q_3 + q_0q_2) & 2(q_2q_3 - q_0q_1) & q_0^2 - q_1^2 - q_2^2 + q_3^2 \end{bmatrix} \quad \text{(A14)}$$

3. Implementation

We refer to Ref. [67] for our GPU-based highly parallelized implementation of the MPC algorithm. We use the average MPC fluid particle density (particles per collision cell) $\langle N_c\rangle = 20$, the collision time $h = 0.02a\sqrt{m/(k_{\mathrm{B}}T)}$, and the rotation angle $\alpha = 130^\circ$, which yield the fluid viscosity $\eta = 42.6\sqrt{mk_{\mathrm{B}}T}/a^2$ [65,89]. With the squirmer radius $R_{\mathrm{sq}} = 3a$, these MPC parameters give the rotational diffusion coefficient $D_R = 4.1\times10^{-5}\sqrt{k_{\mathrm{B}}T/m}/a$.

APPENDIX B: STERIC SQUIRMER INTERACTION

Steric repulsion between two squirmers is described by the separation-shifted Lennard-Jones potential

$$U_{\mathrm{LJ}}(d_s) = 4\epsilon_0\left[\left(\frac{\sigma_0}{d_s+\sigma_0}\right)^{12} - \left(\frac{\sigma_0}{d_s+\sigma_0}\right)^{6} + \frac{1}{4}\right], \quad \text{(B1)}$$

for $d_s < (2^{1/6} - 1)\sigma_0$ and zero otherwise, where d_s indicates the surface-to-surface distance between the two squirmers. To avoid loss of hydrodynamic interactions when two squirmers contact each other, we also include a virtual safety distance d_v [20,82], which leads to the effective distance $d_s = r_c - \sigma - 2d_v$, where r_c denotes the center-to-center distance, and σ is the squirmer diameter. We choose $\sigma_0 = 2d_v$. Numerically, the equations of motion for the rigid-body dynamics of the squirmers are solved by the velocity-Verlet algorithm.

APPENDIX C: ESTIMATION OF MICROSWIMMER PARAMETERS

Various characteristics of microswimmers have been experimentally determined. The tumbling dynamics of *E. coli* bacteria [29,90] and the active turning motion of uniflagellate *Chlamydomonas reinhardtii* [91] as well the zoospore of *Phytophthora parasitica* have been analyzed [92]. The latter

TABLE I. Various experimental characteristics of *E. coli* bacteria, eukaryotic microswimmers *Chlamydomonas* and *Phytophthora*, and microbots. Typical values for the average radius R, swim speed v_0, thermal rotational diffusion coefficient D_R, angular velocity ω, maneuverability $\Omega = C_0/D_R$, Péclet number $\mathrm{Pe} = v_0/(2RD_R)$, and ratio $\Omega/\mathrm{Pe} = 2C_0R/v_0$. For the biohybrid swimmer, we use $R = R_s$ in Ω/Pe (see Appendix D).

	$R/\,\mu\mathrm{m}$	$v_0/(\,\mu\mathrm{m}/s)$	$D_R/(\mathrm{rad}^2/s)$	$C_0/(\mathrm{rad}/s)$	Pe	Ω	Ω/Pe	Ref.
E. coli	1.5	25	5.7×10^{-2}	5	146	88	0.60	[29,90]
Chlamydomonas	4	50	2.6×10^{-3}	25	2.4×10^3	9.6×10^3	4.0	[91]
Phytophthora	5	150	1.5×10^{-3}	2	10^4	1.3×10^3	0.13	[92]
Janus colloid	3	0.6	6×10^{-3}	0.06	17	10	0.6	[93]
Biohybrid microbot:							0.12	[94]
Subunit	7	2	4.7×10^{-4}		213			
Dumbbell	10	2	1.6×10^{-4}	1.7×10^{-2}		109		

can turn on the spot by breaststrokelike flagellar beating. In addition, the active control of the motion of both synthetic Janus particles [93] and biohybrid microbots [94] has been demonstrated for translational and rotational motion. According to Eq. (5), the maximum angular velocity of the squirmer is given by $|\boldsymbol{\omega}| = C_0$ for $\mathbf{e} \perp \mathbf{e}_{\mathrm{aim}}$, which links the angular velocity with our parameter C_0. Table I summarizes the experimental values.

E. coli: The data for the swim velocity and the radius are taken from Ref. [29]. In the calculation of the Péclet number, we use the radius $R = 1.5\,\mu\mathrm{m}$ because of the wobbling dynamics of *E. coli* [95–97], which increases its cross-section in the swim direction. The angular velocity has been extracted from the experimental data presented in Ref. [90].

Chlamydomonas: Data are represented for the *uni1* mutant strain with one flagellum only, which rotates approximately in place.

Phytophthora zoospore: The zoospore has two flagella, one in front and one near the posterior pole. During swimming, the two flagella beat sinusoidally. During local rotation, the posterior flagellum stops, and the anterior flagellum changes its beating pattern to breast-strokelike motion, as *Chlamydomonas*.

Janus colloid: Propulsion in binary liquid mixture is near the demixing critical point; actuation is by temperature change from a focused laser beam. The rotational diffusion coefficient is estimated for a colloid in water.

Biohybrid microbot: Two blocks with eight adhering and propelling bacteria each are rigidly connected by a linker bar. Bacteria activity is controlled by a focused laser beam. The passive diffusion coefficient is estimated for a sphere of equal diameter.

APPENDIX D: STEERABLE TWIN-ENGINE MICROSWIMMERS

Several steerable microswimmers can be described by a passive body with two identical propulsion engines on sides. Examples are *Chlamydomonas* with two beating flagella [98] and the biohybrid swimmer of Ref. [94], with two blocks with attached bacteria connected by a bar, which are individually stimulated by light. A simple toy model for such a swimmer is illustrated in Fig. 7. This model swimmer is propelled on a straight line when both engines are on and generate the same propulsion force f_0, whereas the swimmer rotates around its center of mass when only one engine is on and the other is off. With rotational and translational friction coefficients of a sphere of radius R_b and distance of the force action at a distance R_a from the center, the ratio of maneuverability and Péclet number can be easily calculated to be

$$\Omega/\mathrm{Pe} = \left(\tfrac{3}{4}\right) R_b/R_a < 1. \tag{D1}$$

A closely related model consists of two spherical particles of radius R_s, which can both be propelled or not propelled with speed v_0, in a dumbbell-like configuration with a rigid linker of length $2R_l$ [94]. With the Péclet number defined for the subunit, we find in this case (ignoring the rotational friction of the spherical subunits)

$$\Omega/\mathrm{Pe} = R_s/R_l < 1. \tag{D2}$$

These calculations show for such twin-engine swimmers the ratio Ω/Pe is (i) independent of the propulsion force f_0 and (ii) takes a value of order unity or smaller (as typically $R_a \gtrsim R_b$ and $R_l > R_s$). The estimates of Ω/Pe are in good agreement with the values for real-world microswimmers collected in Table I.

APPENDIX E: SPATIAL CORRELATION AND ENERGY SPECTRUM

1. Squirmers: Particle-based approach

The spatial velocity correlation function of the squirmers is defined as

$$C_{\mathrm{sq}}(r) = \frac{1}{\bar{v}^2} \frac{\left\langle \sum_{i \neq j} \mathbf{v}_i \cdot \mathbf{v}_j \delta(r - |\mathbf{r}_i - \mathbf{r}_j|) \right\rangle}{\left\langle \sum_{i \neq j} \delta(r - |\mathbf{r}_i - \mathbf{r}_j|) \right\rangle}, \tag{E1}$$

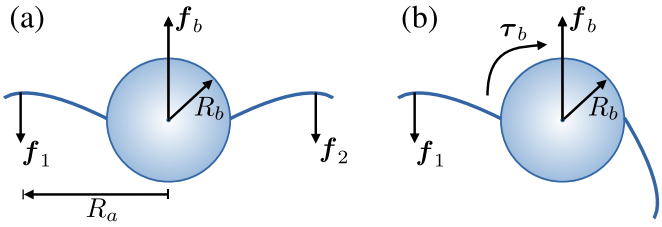

FIG. 7. Illustration of a steerable twin-engine microswimmer, which is capable of swimming with two modes: straight motion (both engines on, $f_1 = f_2 = f_0$) and turning (one engine on, the other off, $f_1 = f_0$, $f_2 = 0$, which generates a torque $\tau_b = f_0 R_a$).

where $\bar{v}^2 \equiv (\sum_i |\mathbf{v}_i|^2/N)$. Here, we use the velocity averaged over a short time interval Δt, for which we consider $\Delta t = 0.26\sigma/v_0$, to reduce the influence of thermal fluctuations. The energy spectrum can be calculated via Fourier transformation. Here, we consider the Fourier sine transform [99]

$$E_{\rm sq}(k) = \frac{k}{\pi}\int {\rm d}r\, r \sin kr\, \bar{v}^2 C_{\rm sq}(r). \tag{E2}$$

2. Fluid: Field-based approach

We first extract the fluid velocity field $\mathbf{v}_{\rm fl}$ from the simulation data by introducing a grid dividing the whole system into N_g^3 cells. The velocities of all MPC particles, averaged over a short time interval Δt as for squirmers, are additionally averaged over each cell to obtain $\mathbf{v}_{\mathbf{n}}$ with $\mathbf{n} = (n_x, n_y, n_z)^T$ for $n_i = 0, \ldots, N_g - 1$ and $i \in \{x, y, z\}$. Then the discrete Fourier transform

$$\mathbf{v}_{\rm fl}(\mathbf{k}) = \frac{1}{N_g^3}\sum_{\mathbf{n}} \mathbf{v}_{\rm sq}(\mathbf{n}) \exp(i2\pi a\mathbf{k}\cdot\mathbf{n}/N_g) \tag{E3}$$

is performed. The three-dimensional energy spectrum is calculated straightforwardly via [100]

$$E_{\rm fl}(\mathbf{k}) = \tfrac{1}{2}|\mathbf{v}_{\rm fl}(\mathbf{k})|^2, \tag{E4}$$

which is then averaged over all directions of $\mathbf{k}$ to obtain $E_{\rm fl}(k)$. We note that the discrete Fourier transform must be multiplied by a spatial spacing, e.g., a, to match the physical dimensions of continuous Fourier transform [71]. The spatial velocity correlation function is obtained via the Fourier transformation

$$C_v(\mathbf{n}) = \sum_{\mathbf{n}} \langle E_{\rm fl}(\mathbf{k})\rangle \exp(-i2\pi a\mathbf{k}\cdot\mathbf{n}/N_g), \tag{E5}$$

from which we calculate $C_{\rm fl}(r)$ by averaging over all directions of $\mathbf{n}$. To reduce noise effects at small length scales, velocity fields are averaged over boxes with side lengths σ, 2σ, or 3σ.

The vorticity field is then defined as

$$\boldsymbol{\omega}(\mathbf{n}) \equiv \nabla_{\mathbf{n}} \times \mathbf{v}_{\rm fl}(\mathbf{n}). \tag{E6}$$

Numerically, the vorticity field is calculated by the five-point stencil method from the velocity field. The vorticity spatial correlations C_ω are also obtained from Eqs. (E3)–(E5). Moreover, a gliding time average is performed for the velocity with a time window Δt, corresponding to $v_0\Delta t \approx 0.26\sigma$.

3. Cross-correlation

We again utilize Fourier transformation to calculate cross-correlations between velocity and vorticity fields. Specifically, we first calculate the magnitudes of velocity and vorticity fields, which are then shifted by their average values, i.e., $\tilde{v}(\mathbf{n}) \equiv v(\mathbf{n}) - \sum_{\mathbf{n}} v(\mathbf{n})/N_g^3$ and $\tilde{\omega}(\mathbf{n}) \equiv \omega(\mathbf{n}) - \sum_{\mathbf{n}} \omega(\mathbf{n})/N_g^3$. Then from the Fourier transforms of the fields $\tilde{v}(\mathbf{k})$ and $\tilde{\omega}(\mathbf{k})$, the cross-correlation is obtained via

$$C_{v\omega}(\mathbf{n}) = \sum_{\mathbf{n}} \langle \tilde{v}(\mathbf{k})\tilde{\omega}^*(\mathbf{k})\rangle \exp(-i2\pi a\mathbf{k}\cdot\mathbf{n}/N_g), \tag{E7}$$

where superscript $*$ indicates the complex conjugate, and $C_{v\omega}(r)$ is obtained by averaging over all $\mathbf{n}$ directions.

APPENDIX F: ENERGY SPECTRUM OF THERMAL FLUCTUATIONS

As discussed in Ref. [73], the equal-time spatial velocity correlation function of an MPC fluid is given by

$$\langle \mathbf{v}(\mathbf{r})\cdot\mathbf{v}(\mathbf{r}')\rangle = \frac{3k_{\rm B}Ta^3}{m\langle N_c\rangle}\delta(\mathbf{r}-\mathbf{r}'), \tag{F1}$$

corresponding to the equipartition of kinetic energy. The Fourier transform of Eq. (F1) reads

$$|\mathbf{v}(\mathbf{k})|^2 = \frac{1}{(2\pi)^3}\frac{3k_{\rm B}Ta^3}{mN_c}, \tag{F2}$$

and therefore,

$$E(k) = \frac{3k_{\rm B}Ta^3}{4\pi^2 mN_c}k^2, \tag{F3}$$

which is the energy spectrum of thermal fluctuations.

In our simulations, we also observe the k^2 scaling for large k. To highlight the dynamical behavior of thermal fluctuations, no average over a time interval is applied in contrast with the discussion in Appendix E. The energy spectrum of thermal noise should also depend on the considered length scales, namely, the length over which velocities of MPC particles are averaged. For small length scales, comparable with or smaller than a single MPC cell, the energy spectrum may deviate from that of thermal fluctuations as MPC particles within the same MPC cell develop correlations during collision steps. On the other hand, if the velocities are averaged over a large length scale, the energy spectrum will also be affected. As shown in Fig. 8(a), we observe a good agreement between the

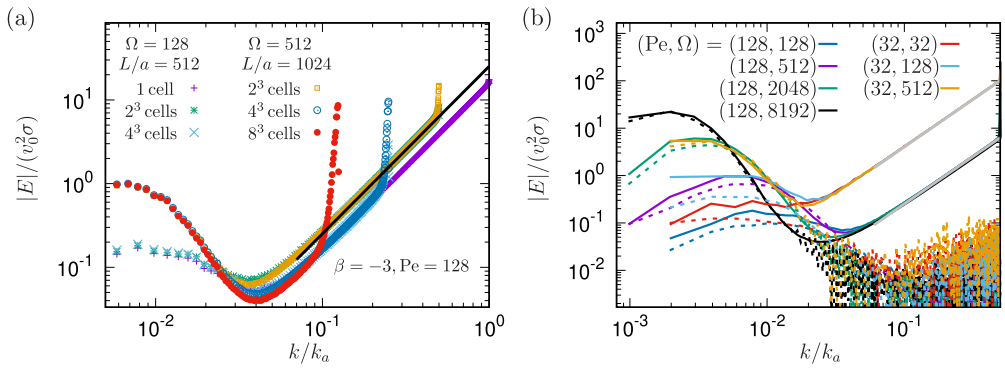

FIG. 8. Energy spectrum of thermal fluctuations. The black solid line in (a) and gray solid lines in (b) represent the theoretical prediction of Eq. (F3). Here, $L = 1024a$ and $512a$ are used for Pe = 128 and 32, respectively, and $k_a \equiv 2\pi/a$.

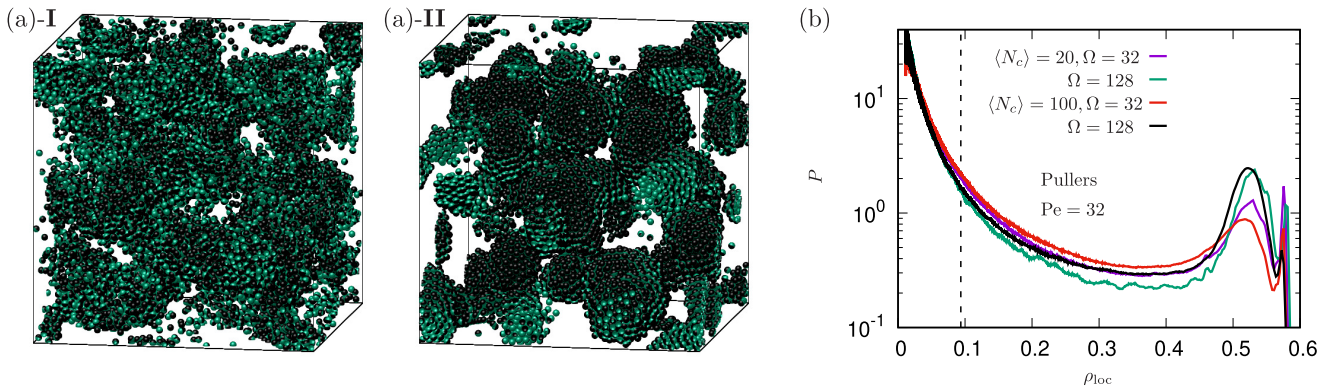

FIG. 9. Cluster formation in puller systems. Snapshots of appearing structures are shown for (a)-I Pe = 128, Ω = 128 and (a)-II Pe = 128, Ω = 512. (b) Local density distribution for Pe = 32, Ω = 32 and Pe = 32, Ω = 128. The average multiparticle collision dynamics (MPC) particle numbers $\langle N_c\rangle = 20$ and 100 are used, as indicated.

theoretical prediction [Eq. (F3)] and the simulation results of the fluid energy energy spectra for $k/k_a \gtrsim 0.1$, if the velocities of MPC particles are averaged over 2^3 cells. Accordingly, in Fig. 8(b), energy spectra obtained from the fluid and squirmer velocities averaged over 2^3 MPC cells are presented for various parameter sets, together with the theoretical prediction.

APPENDIX G: PULLERS—STATIONARY CLUSTER FORMATION

As shown in Fig. 9(a), static clusters emerge in puller systems for Ω = Pe and Ω = 4 Pe, with Pe = 32 and 128. The corresponding local density distributions exhibit a third peak at high densities $\rho_{\rm loc} \approx 0.58$, as shown in Fig. 9(b). As we have introduced a virtual safety distance $d_v = 0.25a$ (see Appendix B), the corresponding effective volume fraction in terms of the effective radius $R_{\rm sq} + d_v$ yields 0.74, indicating the existence of face-centered cubic structure within clusters, which we attribute to fluid depletion due to MPC compressibility [66]. The height of that peak reduces substantially, when we increase the MPC particle density to $\langle N_c\rangle = 100$ for Pe = 32. This indicates that it is most likely a comprehensibility effect of the MPC fluid and that it would vanish for even higher MPC particle densities [66]. We emphasize, however, that for the Ω-to-Pe ratio values other than those discussed in this section (Ω/Pe = 1, 4), puller clusters

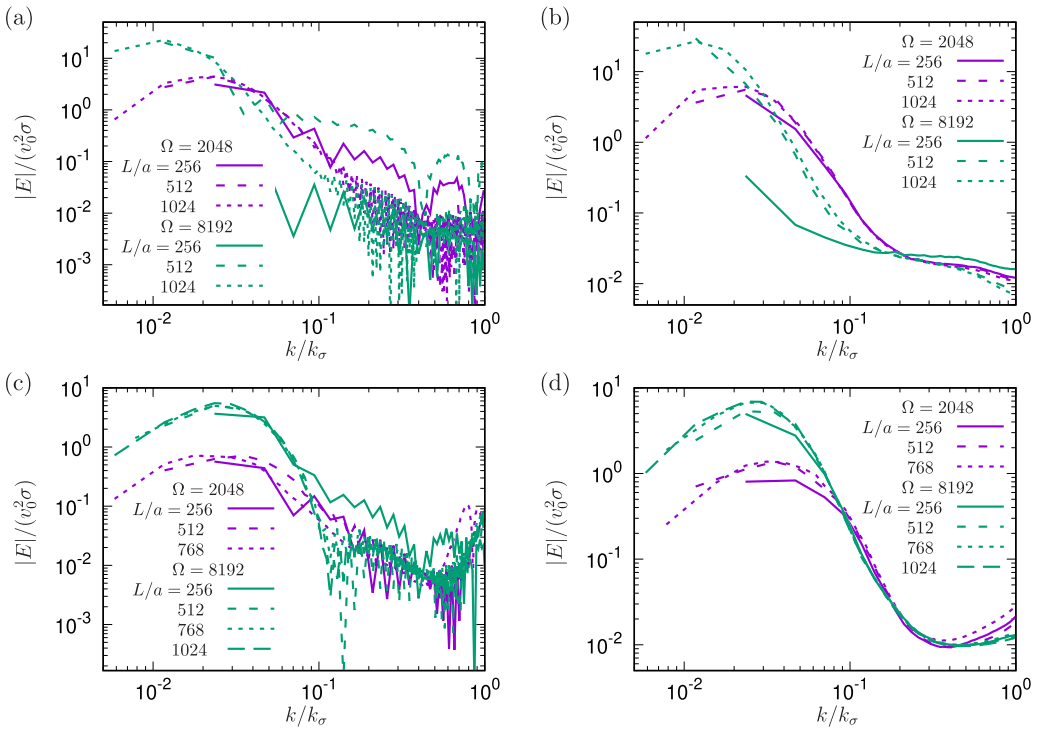

FIG. 10. (a) and (c) Squirmer and (b) and (d) fluid energy spectra for pusher (upper panel) and puller (lower panel) systems with Ω = 2048 and 8192 and various system sizes L/a = 256, 512, 768, and 1024, as indicated.

are highly dynamic and therefore not suffering from this compressibility issue, as confirmed by the absence of the high density peak [Fig. 3(b)].

APPENDIX H: FINITE-SIZE EFFECTS

Figure 10 displays the dependence of the squirmer and fluid energy spectrum on the system size L. We first notice that the increase of $|E|$ as k increases for $k/k_\sigma \lesssim 0.02$ is not visible in the energy spectrum for small system sizes, indicating the presence of finite-size effects. The largest system size employed for respective parameters indeed captures the full picture of the dynamics, including large length scales, confirming that finite-size effects are small.

Notably, the squirmer energy spectra exhibit seemingly artificial oscillatory behavior for small system sizes. In this case, $|E(k)|$ is obtained as the inverse Fourier transform of the spatial correlation function, which is essentially limited to half of the system size $L/2$. Therefore, if the squirmer correlation function C_{sq}, defined in Eq. (E1), does not decay to zero within $L/2$, an artificial discontinuity in C_{sq} due to the small system size eventually affects the inverse Fourier transform. Only for a large system size does C_{sq} decay to zero within half of the simulation box, and the oscillations disappear. In contrast, the fluid energy spectrum is directly obtained via the fluid velocity field [Eq. (E4)], which is a periodic function in space. In this case, finite-size effects only manifest for small k. Therefore, the fluid energy spectra may still exhibit the correct scaling behavior in the intermediate regime around $k/k_\sigma \approx 0.1$ even for small system sizes, except for $L/a = 256$ and $\Omega = 8192$ for pushers. For the latter, the decay of the correlation function [Fig. 2(b)] indicates that the typical vortex size already exceeds the system size. Otherwise, the scaling behavior barely depends on the system size L.

[1] T. J. Pedley and J. O. Kessler, Hydrodynamic phenomena in suspensions of swimming microorganisms, Annu. Rev. Fluid Mech. **24**, 313 (1992).

[2] A. Be'er and G. Ariel, A statistical physics view of swarming bacteria, Mov. Ecol. **7**, 9 (2019).

[3] Y. Katz, K. Tunstrøm, C. C. Ioannou, C. Huepe, and I. D. Couzin, Inferring the structure and dynamics of interactions in schooling fish, Proc. Natl. Acad. Sci. USA **108**, 18720 (2011).

[4] J. Gautrais, F. Ginelli, R. Fournier, S. Blanco, M. Soria, H. Chaté, and G. Theraulaz, Deciphering interactions in moving animal groups, PLOS Comput. Biol. **8**, e1002678 (2012).

[5] M. Ballerini, N. Cabibbo, R. Candelier, A. Cavagna, E. Cisbani, I. Giardina, A. Orlandi, G. Parisi, A. Procaccini, M. Viale *et al.*, Empirical investigation of starling flocks: A benchmark study in collective animal behaviour, Anim. Behav. **76**, 201 (2008).

[6] W. Bialek, A. Cavagna, I. Giardina, T. Mora, E. Silvestri, M. Viale, and A. M. Walczak, Statistical mechanics for natural flocks of birds, Proc. Natl. Acad. Sci. USA **109**, 4786 (2012).

[7] D. Helbing, I. Farkas, and T. Vicsek, Simulating dynamical features of escape panic, Nature (London) **407**, 487 (2000).

[8] H. Xie, M. Sun, X. Fan, Z. Lin, W. Chen, L. Wang, L. Dong, and Q. He, Reconfigurable magnetic microrobot swarm: Multimode transformation, locomotion, and manipulation, Sci. Robot. **4**, eaav8006 (2019).

[9] Q. Wang, K. F. Chan, K. Schweizer, X. Du, D. Jin, S. C. H. Yu, B. J. Nelson, and L. Zhang, Ultrasound doppler-guided real-time navigation of a magnetic microswarm for active endovascular delivery, Sci. Adv. **7**, eabe5914 (2021).

[10] C.-J. Chen and C. Bechinger, Collective response of microrobotic swarms to external threats, New J. Phys. **24**, 033001 (2022).

[11] X. Wang, P.-C. Chen, K. Kroy, V. Holubec, and F. Cichos, Spontaneous vortex formation by microswimmers with retarded attractions, Nat. Commun. **14**, 56 (2023).

[12] E. Lauga and T. R. Powers, The hydrodynamics of swimming microorganisms, Rep. Prog. Phys. **72**, 096601 (2009).

[13] D. L. Koch and G. Subramanian, Collective hydrodynamics of swimming microorganisms: Living fluids, Annu. Rev. Fluid Mech. **43**, 637 (2011).

[14] J. Elgeti, R. G. Winkler, and G. Gompper, Physics of microswimmers—Single particle motion and collective behavior: A review, Rep. Prog. Phys. **78**, 056601 (2015).

[15] G. Gompper *et al.*, The 2020 motile active matter roadmap, J. Phys: Condens. Matter **32**, 193001 (2020).

[16] H. Chaté, Dry aligning dilute active matter, Annu. Rev. Condens. Matter Phys. **11**, 189 (2020).

[17] Y. Fily and M. C. Marchetti, Athermal phase separation of self-propelled particles with no alignment, Phys. Rev. Lett. **108**, 235702 (2012).

[18] I. Buttinoni, J. Bialké, F. Kümmel, H. Löwen, C. Bechinger, and T. Speck, Dynamical clustering and phase separation in suspensions of self-propelled colloidal particles, Phys. Rev. Lett. **110**, 238301 (2013).

[19] H. H. Wensink, J. Dunkel, S. Heidenreich, K. Drescher, R. E. Goldstein, H. Löwen, and J. M. Yeomans, Meso-scale turbulence in living fluids, Proc. Natl. Acad. Sci. USA **109**, 14308 (2012).

[20] K. Qi, E. Westphal, G. Gompper, and R. G. Winkler, Emergence of active turbulence in microswimmer suspensions due to active hydrodynamic stress and volume exclusion, Commun. Phys. **5**, 49 (2022).

[21] I. S. Aranson, Bacterial active matter, Rep. Prog. Phys. **85**, 076601 (2022).

[22] A. Ziepke, I. Maryshev, I. S. Aranson, and E. Frey, Multi-scale organization in communicating active matter, Nat. Commun. **13**, 6727 (2022).

[23] J. Sawicki *et al.*, Perspectives on adaptive dynamical systems, Chaos **33**, 071501 (2023).

[24] R. S. Negi, R. G. Winkler, and G. Gompper, Collective behavior of self-steering active particles with velocity alignment and visual perception, Phys. Rev. Res. **6**, 013118 (2024).

[25] S. Ceron, G. Gardi, K. Petersen, and M. Sitti, Programmable self-organization of heterogeneous microrobot collectives, Proc. Natl. Acad. Sci. USA **120**, e2221913120 (2023).

[26] I. Llopis and I. Pagonabarraga, Hydrodynamic interactions in squirmer motion: Swimming with a neighbour and close to a wall, J. Non-Newtonian Fluid Mech. **165**, 946 (2010).

[27] J. Clopés, G. Gompper, and R. G. Winkler, Hydrodynamic interactions in squirmer dumbbells: Active stress-induced alignment and locomotion, Soft Matter **16**, 10676 (2020).

[28] C. Dombrowski, L. Cisneros, S. Chatkaew, R. E. Goldstein, and J. O. Kessler, Self-concentration and large-scale coherence in bacterial dynamics, Phys. Rev. Lett. **93**, 098103 (2004).

[29] K. Drescher, J. Dunkel, L. H. Cisneros, S. Ganguly, and R. E. Goldstein, Fluid dynamics and noise in bacterial cell-cell and cell-surface scattering, Proc. Natl. Acad. Sci. USA **108**, 10940 (2011).

[30] R. Alert, J. Casademunt, and J.-F. Joanny, Active turbulence, Annu. Rev. Condens. Matter Phys. **13**, 143 (2022).

[31] V. E. Deneke, A. Puliafito, D. Krueger, A. V. Narla, A. De Simone, L. Primo, M. Vergassola, S. De Renzis, and S. Di Talia, Self-organized nuclear positioning synchronizes the cell cycle in drosophila embryos, Cell **177**, 925 (2019).

[32] C. Hernández-López, A. Puliafito, Y. Xu, Z. Lu, S. D. Talia, and M. Vergassola, Two-fluid dynamics and micron-thin boundary layers shape cytoplasmic flows in early *Drosophila* embryos, Proc. Natl. Acad. Sci. USA **120**, e2302879120 (2023).

[33] A. Sokolov and I. S. Aranson, Physical properties of collective motion in suspensions of bacteria, Phys. Rev. Lett. **109**, 248109 (2012).

[34] A. W. Zantop and H. Stark, Emergent collective dynamics of pusher and puller squirmer rods: Swarming, clustering, and turbulence, Soft Matter **18**, 6179 (2022).

[35] A. N. Kolmogorov, V. Levin, J. C. R. Hunt, O. M. Phillips, and D. Williams, The local structure of turbulence in incompressible viscous fluid for very large Reynolds numbers, Proc. R. Soc. A **434**, 9 (1991).

[36] A. J. T. M. Mathijssen, T. N. Shendruk, J. M. Yeomans, and A. Doostmohammadi, Upstream swimming in microbiological flows, Phys. Rev. Lett. **116**, 028104 (2016).

[37] J. Arrieta, M. Polin, R. Saleta-Piersanti, and I. Tuval, Light control of localized photobioconvection, Phys. Rev. Lett. **123**, 158101 (2019).

[38] M. A. Bees, Advances in bioconvection, Annu. Rev. Fluid Mech. **52**, 449 (2020).

[39] W. Cheng, S. Hwang, Q. Guo, L. Qian, W. Liu, Y. Yu, L. Liu, Y. Tao, and H. Cao, The special and general mechanism of cyanobacterial harmful algal blooms, Microorganisms **11**, 987 (2023).

[40] J. B. Riding, R. A. Fensome, M.-O. Soyer-Gobillard, and L. K. Medlin, A review of the dinoflagellates and their evolution from fossils to modern, J. Mar. Sci. Eng. **11**, 1 (2023).

[41] A. Sengupta, F. Carrara, and R. Stocker, Phytoplankton can actively diversify their migration strategy in response to turbulent cues, Nature (London) **543**, 555 (2017).

[42] J. Toner and Y. Tu, Flocks, herds, and schools: A quantitative theory of flocking, Phys. Rev. E **58**, 4828 (1998).

[43] D. Saintillan and M. J. Shelley, Instabilities and pattern formation in active particle suspensions: Kinetic theory and continuum simulations, Phys. Rev. Lett. **100**, 178103 (2008).

[44] T. Vicsek, A. Czirók, E. Ben-Jacob, I. Cohen, and O. Shochet, Novel type of phase transition in a system of self-driven particles, Phys. Rev. Lett. **75**, 1226 (1995).

[45] C. Bechinger, R. Di Leonardo, H. Löwen, C. Reichhardt, G. Volpe, and G. Volpe, Active particles in complex and crowded environments, Rev. Mod. Phys. **88**, 045006 (2016).

[46] H. Reinken, S. H. L. Klapp, M. Bär, and S. Heidenreich, Derivation of a hydrodynamic theory for mesoscale dynamics in microswimmer suspensions, Phys. Rev. E **97**, 022613 (2018).

[47] Z. T. Liu, Y. Shi, Y. Zhao, H. Chaté, X.-Q. Shi, and T. H. Zhang, Activity waves and freestanding vortices in populations of subcritical Quincke rollers, Proc. Natl. Acad. Sci. USA **118**, e2104724118 (2021).

[48] R. A. Simha and S. Ramaswamy, Hydrodynamic fluctuations and instabilities in ordered suspensions of self-propelled particles, Phys. Rev. Lett. **89**, 058101 (2002).

[49] I. O. Götze and G. Gompper, Mesoscale simulations of hydrodynamic squirmer interactions, Phys. Rev. E **82**, 041921 (2010).

[50] J. Dunkel, S. Heidenreich, K. Drescher, H. H. Wensink, M. Bär, and R. E. Goldstein, Fluid dynamics of bacterial turbulence, Phys. Rev. Lett. **110**, 228102 (2013).

[51] H. Meyer and H. Rieger, Alignment interaction and band formation in assemblies of autochemorepulsive walkers, Phys. Rev. E **108**, 034604 (2023).

[52] S. Goh, R. G. Winkler, and G. Gompper, Hydrodynamic pursuit by cognitive self-steering microswimmers, Commun. Phys. **6**, 310 (2023).

[53] M. J. Lighthill, On the squirming motion of nearly spherical deformable bodies through liquids at very small Reynolds numbers, Comm. Pure Appl. Math. **5**, 109 (1952).

[54] J. R. Blake, A spherical envelope approach to ciliary propulsion, J. Fluid Mech. **46**, 199 (1971).

[55] T. Ishikawa, M. P. Simmonds, and T. J. Pedley, Hydrodynamic interaction of two swimming model micro-organisms, J. Fluid Mech. **568**, 119 (2006).

[56] M. Theers, E. Westphal, G. Gompper, and R. G. Winkler, Modeling a spheroidal microswimmer and cooperative swimming in a narrow slit, Soft Matter **12**, 7372 (2016).

[57] O. S. Pak and E. Lauga, Generalized squirming motion of a sphere, J. Eng. Math. **88**, 1 (2014).

[58] A. Malevanets and R. Kapral, Mesoscopic model for solvent dynamics, J. Chem. Phys. **110**, 8605 (1999).

[59] R. Kapral, Multiparticle collision dynamics: Simulations of complex systems on mesoscale, Adv. Chem. Phys. **140**, 89 (2008).

[60] G. Gompper, T. Ihle, D. M. Kroll, and R. G. Winkler, Multi-particle collision dynamics: A particle-based mesoscale simulation approach to the hydrodynamics of complex fluids, Adv. Polym. Sci. **221**, 1 (2009).

[61] M. R. Shaebani, A. Wysocki, R. G. Winkler, G. Gompper, and H. Rieger, Computational models for active matter, Nat. Rev. Phys. **2**, 181 (2020).

[62] S. Goh, R. G. Winkler, and G. Gompper, Noisy pursuit and pattern formation of self-steering active particles, New J. Phys. **24**, 093039 (2022).

[63] O. Chepizhko, D. Saintillan, and F. Peruani, Revisiting the emergence of order in active matter, Soft Matter **17**, 3113 (2021).

[64] A. Bera, S. Sahoo, S. Thakur, and S. K. Das, Active particles in explicit solvent: Dynamics of clustering for alignment interaction, Phys. Rev. E **105**, 014606 (2022).

[65] H. Noguchi and G. Gompper, Transport coefficients of off-lattice mesoscale-hydrodynamics simulation techniques, Phys. Rev. E **78**, 016706 (2008).

[66] M. Theers, E. Westphal, K. Qi, R. G. Winkler, and G. Gompper, Clustering of microswimmers: Interplay of shape and hydrodynamics, Soft Matter **14**, 8590 (2018).

[67] E. Westphal, S. Goh, R. G. Winkler, and G. Gompper, HTMPC: A heavily templated C++ library for large scale particle-based mesoscale hydrodynamics simulations using multiparticle collision dynamics, Comput. Phys. Commun. **309**, 109494 (2025).

[68] See Supplemental Material at http://link.aps.org/supplemental/10.1103/PhysRevResearch.7.013142 for Movies S1–S6.

[69] C. H. Rycroft, VORO++: A three-dimensional Voronoi cell library in C++, Chaos **19**, 041111 (2009).

[70] D. Saintillan and M. J. Shelley, Orientational order and instabilities in suspensions of self-locomoting rods, Phys. Rev. Lett. **99**, 058102 (2007).

[71] Z. Liu, W. Zeng, X. Ma, and X. Cheng, Density fluctuations and energy spectra of 3D bacterial suspensions, Soft Matter **17**, 10806 (2021).

[72] D. Bárdfalvy, H. Nordanger, C. Nardini, A. Morozov, and J. Stenhammar, Particle-resolved lattice Boltzmann simulations of 3-dimensional active turbulence, Soft Matter **15**, 7747 (2019).

[73] C.-C. Huang, G. Gompper, and R. G. Winkler, Hydrodynamic correlations in multiparticle collision dynamics fluids, Phys. Rev. E **86**, 056711 (2012).

[74] Y.-E. Keta, J. U. Klamser, R. L. Jack, and L. Berthier, Emerging mesoscale flows and chaotic advection in dense active matter, Phys. Rev. Lett. **132**, 218301 (2024).

[75] A. Gascó, I. Pagonabarraga, and A. Scagliarini, Three-dimensional active turbulence in microswimmer suspensions: simulations and modelling, arXiv:2304.03662.

[76] V. M. Worlitzer, G. Ariel, A. Be'er, H. Stark, M. Baer, and S. Heidenreich, Motility-induced clustering and meso-scale turbulence in active polar fluids, New J. Phys. **23**, 033012 (2021).

[77] V. M. Worlitzer, G. Ariel, A. Be'er, H. Stark, M. Bär, and S. Heidenreich, Turbulence-induced clustering in compressible active fluids, Soft Matter **17**, 10447 (2021).

[78] www.gauss-centre.eu.

[79] Jülich Supercomputing Centre, JUWELS Cluster and Booster: Exascale pathfinder with modular supercomputing architecture at Juelich Supercomputing Centre, JLSRF **7**, A183 (2021).

[80] Simulation data are available on the Zenodo repository [81] for two exemplary parameters sets, one for pullers and one for pushers, together with evaluation scripts for data analysis. Additional data are available from the authors upon reasonable request.

[81] https://doi.org/10.5281/zenodo.14649945.

[82] M. Theers, E. Westphal, G. Gompper, and R. G. Winkler, From local to hydrodynamic friction in Brownian motion: A multiparticle collision dynamics simulation study, Phys. Rev. E **93**, 032604 (2016).

[83] C.-C. Huang, A. Chatterji, G. Sutmann, G. Gompper, and R. G. Winkler, Cell-level canonical sampling by velocity scaling for multiparticle collision dynamics simulations, J. Comput. Phys. **229**, 168 (2010).

[84] A. Lamura, G. Gompper, T. Ihle, and D. M. Kroll, Multiparticle collision dynamics: Flow around a circular and a square cylinder, Europhys. Lett. **56**, 319 (2001).

[85] C.-C. Huang, A. Varghese, G. Gompper, and R. G. Winkler, Thermostat for nonequilibrium multiparticle-collision-dynamics simulations, Phys. Rev. E **91**, 013310 (2015).

[86] I. P. Omelyan, Algorithm for numerical integration of the rigid-body equations of motion, Phys. Rev. E **58**, 1169 (1998).

[87] K. Qi, E. Westphal, G. Gompper, and R. G. Winkler, Enhanced rotational motion of spherical squirmer in polymer solutions, Phys. Rev. Lett. **124**, 068001 (2020).

[88] J. T. Padding, A. Wysocki, H. Löwen, and A. A. Louis, Stick boundary conditions and rotational velocity auto-correlation functions for colloidal particles in a coarse-grained representation of the solvent, J. Phys.: Condens. Matter **17**, S3393 (2005).

[89] M. Theers and R. G. Winkler, Bulk viscosity of multiparticle collision dynamics fluids, Phys. Rev. E **91**, 033309 (2015).

[90] J. Saragosti, P. Silberzan, and A. Buguin, Modeling *E. coli* tumbles by rotational diffusion. Implications for chemotaxis, PLoS ONE **7**, e35412 (2012).

[91] P. V. Bayly, B. L. Lewis, E. C. Ranz, R. J. Okamoto, R. B. Pless, and S. K. Dutcher, Propulsive forces on the flagellum during locomotion of *Chlamydomonas reinhardtii*, Biophys. J. **100**, 2716 (2011).

[92] Q. D. Tran, E. Galiana, P. Thomen, C. Cohen, F. Orange, F. Peruani, X. Noblin, R. E. Goldstein, and A. M. Walczak, Coordination of two opposite flagella allows high-speed swimming and active turning of individual zoospores, eLife **11**, e71227 (2022).

[93] V.-L. Heuthe, E. Panizon, H. Gu, and C. Bechinger, Counterfactual rewards promote collective transport using individually controlled swarm microrobots, Sci. Robot. **9**, eado5888 (2024).

[94] N. Pellicciotta, O. S. Bagal, V. C. Sosa, G. Frangipane, G. Vizsnyiczai, and R. D. Leonardo, Light controlled biohybrid microbots, Adv. Funct. Mater. **33**, 2214801 (2023).

[95] Y. Hyon, Marcos, T. R. Powers, R. Stocker, and H. C. Fu, The wiggling trajectories of bacteria, J. Fluid Mech. **705**, 58 (2012).

[96] S. Bianchi, F. Saglimbeni, and R. Di Leonardo, Holographic imaging reveals the mechanism of wall entrapment in swimming bacteria, Phys. Rev. X **7**, 011010 (2017).

[97] S. M. Mousavi, G. Gompper, and R. G. Winkler, Wall entrapment of peritrichous bacteria: A mesoscale hydrodynamics simulation study, Soft Matter **16**, 4866 (2020).

[98] T. J. Pedley and J. O. Kessler, A new continuum model for suspensions of gyrotactic micro-organisms, J. Fluid Mech. **212**, 155 (1990).

[99] G. K. Batchelor, *The Theory of Homogeneous Turbulence* (Cambridge University Press, Cambridge, 1959).

[100] U. Frisch, *Turbulence: The Legacy of A. N. Kolmogorov* (Cambridge University Press, Cambridge, 1995).